Chemical Geology 559 (2021) 119928

Contents lists available at ScienceDirect

Chemical Geology

journal homepage: www.elsevier.com/locate/chemgeo

Experimental variable effects on laser heating of inclusions during Raman spectroscopic analysis

Yuuki Hagiwara [a,*], Kenta Yoshida [b], Akira Yoneda [c], Junji Torimoto [d], Junji Yamamoto [e]

[a] Graduate School of Science, Hokkaido University, Kita 10 Nishi 8, Kita-ku, Sapporo, Hokkaido 060-0810, Japan
[b] Research Institute for Marine Geodynamics, Japan Agency for Marine-Earth Science and Technology (JAMSTEC), 2−15, Natsushimacho, Yokosuka-shi, Kanagawa 237-0061, Japan
[c] Institute for Planetary Materials, Okayama University, Misasa, Tottori 682-0193, Japan
[d] Ore Genesis Research Unit, Project Team for Development of New-Generation Research Protocol for Submarine Resources, Japan Agency for Marine-Earth Science and Technology (JAMSTEC), 2−15, Natsushimacho, Yokosuka-shi, Kanagawa 237-0061, Japan
[e] The Hokkaido University Museum, Kita 10 Nishi 8, Kita-ku, Sapporo, Hokkaido 060-0810, Japan

ARTICLE INFO

Editor: Dr. Balz Kamber

Keywords:
Finite element method
Inclusions
Laser heating
Raman spectroscopy

ABSTRACT

Raman spectroscopy for fluid, melt, and mineral inclusions provides direct insight into the physicochemical conditions of the environment surrounding the host mineral at the time of trapping. However, the obtained Raman spectral characteristics such as peak position are modified because of local temperature enhancement of the inclusions by the excitation laser, which might engender systematic errors and incorrect conclusions if the effect is not corrected. Despite the potentially non-negligible effects of laser heating, the laser heating coefficient (B) (°C/mW) of inclusions has remained unsolved. For this study, we found B from experiments and heat transport simulation to evaluate how various parameters such as experimental conditions, mineral properties, and inclusion geometry affect B of inclusions. To assess the parameters influencing laser heating, we measured B of a total of 19 CO_2-rich fluid inclusions hosted in olivine, orthopyroxene, clinopyroxene, spinel, and quartz. Our results revealed that the measured B of fluid inclusions in spinel is highest (approx. 6 °C/mW) and that of quartz is lowest (approx. 1×10^{-2} °C/mW), consistent with earlier inferences. Our simulation results show that the absorption coefficient of the host mineral is correlated linearly with B. It is the most influential parameter when the absorption coefficient of the host mineral (α_h) is larger than that of an inclusion (α_{inc}). Furthermore, although our results indicate that both the inclusion size and depth have little effect on B if $\alpha_h > \alpha_{inc}$, the thickness and radius of the host mineral slightly influence B. These results suggest that the choice of inclusion size and depth to be analyzed in a given sample do not cause any systematic error in the Raman data because of laser heating, but the host radius and thickness, which can be adjusted to some degree at the time of sample preparation, can cause systematic errors between samples.

Our results demonstrate that, even with laser power of 10 mW, which is typical for inclusion analysis, the inclusion temperature rises to tens or hundreds of degrees during the analysis, depending especially on the host mineral geometry and optical properties. Therefore, correction of the heating effects will be necessary to obtain reliable data from Raman spectroscopic analysis of inclusions. This paper presents some correction methods for non-negligible effects of laser heating.

1. Introduction

Raman spectroscopy is now well established as a versatile tool for inclusion research because of its non-invasive analysis and high spatial resolution. This method has been applied to various fields of inclusion studies: ascertaining the depth provenance of rocks from mineral inclusions (Kohn, 2014), estimation of peak metamorphic temperatures from graphite inclusions (Beyssac et al., 2002), determination of the pre-eruptive volatile contents of magmas from melt inclusions (Moore et al., 2015), and characterization of paleo crust-mantle fluid activities from fluid inclusions (Frezzotti et al., 2012). To extract the physicochemical properties of unknown inclusions from the measured Raman spectra,

* Corresponding author.
E-mail address: hagi@eis.hokudai.ac.jp (Y. Hagiwara).

https://doi.org/10.1016/j.chemgeo.2020.119928
Received 20 June 2020; Received in revised form 15 September 2020; Accepted 14 October 2020
Available online 27 October 2020

experimental calibrations related to spectral features to the *P–V–T–X* properties of fluids or the strains and crystal orientations of minerals have been the subject of many studies (e.g., Frezzotti et al., 2012; Angel et al., 2019). Furthermore, the combined technique of microthermometry and Raman spectroscopy enables accurate estimation of the temperatures of phase transition in situ, even for phases that are difficult to assess under optical observation (e.g., Bakker, 2004). Typically, to obtain Raman spectra of an inclusion having a sufficient signal-to-noise ratio for quantitative analysis, laser power of tens to hundreds of milliwatts is necessary, thereby necessitating focal intensities as high as several gigawatts per square centimeter. Even for analysis of transparent geomaterials, such high excitation energy can lead to non-negligible temperature increments at the focal position because of light absorption by host minerals or inclusions themselves. Such undesired heating at the focus will change Raman spectral features and might engender misinterpretation of the data. However, this important experimental parameter, temperature, has been difficult to control and estimate during Raman spectroscopic analysis because local temperatures behave intricately depending on the sample geometry, experimental conditions, and sample optical and heat transport properties. To interpret the inclusion data obtained by Raman spectroscopy correctly, one must ascertain the temperature of inclusion under the analysis and clarify how the temperature is governed as functions of experimental, geometrical, and optical parameters.

Although the thermal damage caused by the excitation laser to samples has been a concern especially in the field of bioengineering (e.g., Català et al., 2017), no comprehensive work assessing laser heating effects of small objects hosted in a solid phase, i.e., inclusions, during Raman spectroscopic analysis has been reported to date. Fall et al. (2011) observed the phase transition of CO_2 fluid after laser irradiation. In their experiments, the CO_2-bearing inclusions, for which homogenization temperatures are slightly higher than the ambient temperature, are heated by an excitation laser, being not homogenized during the experiment. Therefore, the effect of laser heating might be negligible (less than <1 °C), at least under their experimental conditions and when using minerals with very small visible light absorption coefficients, such as quartz. However, the absolute value of the temperature rises at a certain laser power (laser heating coefficient (*B*); °C/mW) has persisted as an open problem for inclusion in representative rock-forming minerals, including quartz.

In the field of Earth science, laser-heating effects on the sample are evaluated especially with respect to Raman spectroscopy of a carbonaceous material (RSCM) thermometer that is used widely for estimating peak metamorphic temperatures. Kagi et al. (1994) reported that an appreciable local temperature increase occurs because of absorption of the incident laser by graphite. According to data reported by Kagi et al. (1994), *B* is approx. 1×10^2 °C/mW. In addition, Umeda and Enami (2014) reported that laser power higher than 2 mW would change apparent spectral properties of CM and would provide apparently high peak metamorphic temperature by the RSCM thermometer (see review by Henry et al., 2019). Similar warming effects by transmitted light have been reported for near-infrared microthermometry for fluid inclusions in opaque to translucent minerals (e.g., Casanova et al., 2018). Therefore, depending on the experimental, geometrical, and optical parameters, the inclusions are heated by the laser during Raman spectroscopic analysis. Their local heating alters the Raman spectral properties. Nevertheless, little is known about which parameters strongly affect laser heating.

To ascertain a correct physical picture of laser heating in inclusion, we perform heat transport simulations of an inclusion hosted by a solid phase (mineral) using finite element method, taking special care of the effects of spherical aberration at the air–sample boundary and the entire three-dimensional spatial profile of the focused beam. Based on the model, the effects of various parameters were evaluated. We also report the experimentally determined value of *B* of CO_2-rich fluid inclusions hosted by representative mantle minerals and quartz. Finally, by combining experimental and simulation results, we discuss the effects of the respective parameters on the laser heating of inclusions. Goals of this paper are to ascertain the most influential parameters on the laser heating of inclusions, and to propose favorable analytical procedures under which results obtained from Raman spectroscopy are reliable.

2. Literature review

Other research fields for which *B* has already been determined provide some examples. A field showing particular progress is optical tweezers for microscopic particle manipulation (e.g., Liu et al., 1995). Earlier studies measured temperatures surrounding optically trapped microspheres in water or glycerol during near infrared irradiation. Reportedly, temperature increases are 0.008–0.099 °C/mW. In most cases, determination of local temperature in an optical trap is based on measurement of the viscosity of the liquid (e.g., water) surrounding an optically trapped bead (e.g., silica) rather than a bead itself. By contrast, our target is a fluid inclusion (liquid CO_2) itself, located at the focal point of the laser, which is surrounded by a solid phase (host mineral).

According to earlier studies, one parameter that strongly influences laser heating is the absorption coefficient of the host phase, not of the trapped particle (Liu et al., 1995; Celliers and Conia, 2000; Peterman et al., 2003; Mao et al., 2005; Català et al., 2017). Because the absorption coefficient depends on the wavelength, it also depends on the laser wavelength (Haro-González et al., 2013). Regarding the bead size, two opposing results have been reported: Peterman et al. (2003) asserted that size has no effect on *B*. Also, Català et al. (2017) reported that larger particles suppress laser heating. The distance between the bead and the boundary of solvent and surrounding material, i.e. glass, also affects *B*. In fact, *B* becomes small only when the bead is close to the interface with the glass (Peterman et al., 2003; Català et al., 2017). Based on the model proposed by Mao et al. (2005), *B* is expected to show logarithmic growth with increasing sample thickness. In addition, *B* is correlated linearly with the reciprocal of the thermal conductivity of the liquid (Celliers and Conia, 2000; Peterman et al., 2003; Mao et al., 2005; Català et al., 2017). The specific *B* and measurement methods used for earlier studies are presented in Table S2 of the report by Català et al. (2017).

3. MODEL: Three-dimensional heat transport simulation using finite element method

To clarify the temperature distribution within and around an inclusion when illuminated by excitation laser, we performed heat-transfer simulation by finite element method using a software package: COMSOL Multiphysics. Fig. 1 depicts a laser beam transmitted through the objective lens towards the inclusion. We assumed symmetric disc shape for the host mineral. The disc has H_h thickness and R_h radius. A spherical inclusion with radius of r_{inc} exists at z_{inc} below the top surface of the disc. The actual focal position (= inclusion depth) is given as $z_{inc} = (n_h/n_a)z_1$, where z_1 is the nominal focal position below the sample surface and where n_a and n_h respectively denote the refractive indices of the air and host mineral.

Temperature is in general terms governed by the heat equation

$$\nabla^2 T = \frac{1}{k_h}\frac{\partial T}{\partial t} - \frac{\alpha_h I_{ill}}{K_h}, \quad (1)$$

where k_h (m^2/s) stands for the thermal diffusivity, K_h (W/mK) expresses the thermal conductivity, and α_h denotes the absorption coefficient of host mineral (1/m). Also, I_{ill} (W/m^2) represents the spatial distribution of the focused intensity inside the sample as (e.g., Maruyama and Kanematsu, 2011)

$$I_{ill}(q, L, z_1) = I_0 \left\{ \frac{w_0}{w(L,\ z_1)} \right\}^2 exp\left\{ -\frac{2q^2}{w^2(L,\ z_1)} \right\}, \quad (2)$$

where q (m) represents the radial distance from the optical axis of an

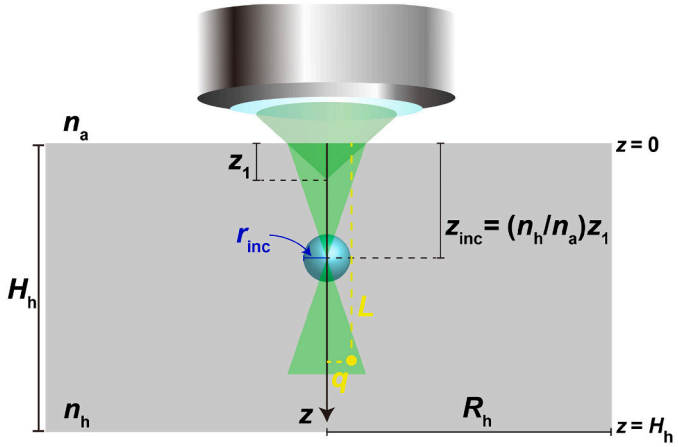

Fig. 1. Schematic of the simulation situation considered in the model. Refractive indices of the host mineral and air are presented respectively as n_h and n_a. The surface (i.e., air–host mineral boundary) of the host mineral is defined as the $z = 0$ plane. The focus position of a transmitted beam shifts from an intended position at $z = z_1$ to $z = (n_h/n_a)z_1$. A blue sphere represents an inclusion with radius of r_{inc} and depth of z_{inc}. q is the radial distance from the optical axis of an illuminated point and L denotes the depth of an illuminated point. The host mineral shape is assumed to be a disc with radius R_h and height H_h. (For interpretation of the references to colour in this figure legend, the reader is referred to the web version of this article.)

illuminated point, L (m) denotes the depth of an illuminated point, and w_0 (m) corresponds to the waist-radius of the laser-beam, where the laser-beam diameter converges to a minimum. The value of w_0 was estimated directly from the Raman instruments used for the measurements. The bitmap image of the laser spot reflected from the silicon wafer surface is used. The estimated w_0 was 1.46 μm for LU Plan ×50 (used at Hokkaido University) and 1.0 μm for TU Plan ×50 (used at Japan Agency for Marine–Earth Science and Technology (JAMSTEC)). Detailed procedures for estimating w_0 are presented in online Supplementary material S1. Also, I_0 (W/m^2) and $w(L, z_1)$ respectively represent the laser intensity at the center of the beam waist and the beam-waist radius at the axial position, given as

$$I_0 = \frac{2P_{ill}}{\pi w_0^2}, \tag{3}$$

$$w\left(L,\ z_1\right) = w_0\sqrt{1 + \left(\frac{L - (n_h/n_a)z_1}{n_h z_0}\right)^2}, \tag{4}$$

where P_{ill} represents the laser power at the sample surface (W) and $z_0 = \pi w_0^2/\lambda$ (m) is the Rayleigh range. Also, λ denotes the excitation laser wavelength.

In an earlier model, the boundary condition which determines heat flux at the interface was the Dirichlet condition (i.e., T = const. at boundaries), but in this study, in addition to the Dirichlet condition, we also performed simulations under convective heat flux boundary condition that is defined by $h(T_{ext} - T)$ at the glass–sample and air–sample interfaces. At the air–sample boundary, the convective heat transfer coefficient ($h_{a/s}$) was fixed to be 5 W/m^{2}K at $z = 0$ plane and $q = R_h$ curved surface, assuming heat transfer by free convection (Whitelaw, 1997). In case of the boundary between the sample and the plate on which the sample is placed ($z = H_h$), it is difficult to settle the style of heat transport because it is affected by many parameters such as surface conditions, optical and heat transport properties of the plate, and the temperature distribution below the sample. Therefore, we considered the heat transport coefficient at the glass–sample interface ($h_{g/s}$) as a variable. Both the ambient (T_{ext}) and initial sample temperature (T_{sample}) are equal. Of the parameters throughout Eqs. (1) to (4), α_h, k_h, K_h, and n_h are optical and physical properties unique to the host mineral and are shown in Table 1. The influence of reflection and crystal orientation dependence of α_h, k_h, K_h, and n_h on the laser heating effect was not considered here.

No report of the relevant literature describes a study of the absorption coefficient of CO_2 at the specific conditions of our simulation, i.e. 532 nm and approx. 7 MPa. Thompson et al. (1963) estimated that absorption coefficient of CO_2 at 198 nm is 10^{-5} cm^{-1}. According to Hansen (1997), absorption coefficient of solid CO_2 at 532 nm is about 10^{-4} cm^{-1}. In both studies, the absorption coefficient decreases as the wavelength increases from approx. 180 nm. The absorption coefficient of CO_2 at 532 nm is so small compared to the host mineral (for the smallest case, e.g., 0.02 cm^{-1} for quartz) that it was regarded as negligible in the present model. Therefore, we assumed it to be 0 (see section 7.1 for details). Thermal diffusivity of CO_2 is 0.02 mm^2/s at the conditions of 0.7 g/cm^3 and 25 °C based on the NIST Chemistry WebBook (Linstrom and Mallard, 2020). The simulated inclusion temperature and B are an average over an inclusion domain in 3D models.

All the parameters used for this study are presented in Table 2. Hereinafter, we use an abbreviation for each parameter. As described in section 2, earlier studies have experimentally or theoretically examined the effects of λ, w_0, α_{inc}, z_{inc}, r_{inc}, K_{inc}, K_h, α_h, H_h, and R_h on B. In addition to these parameters, we investigated the effects of n_h, which can change the temperature distribution around the inclusion, k_h, which affects the time to reach the steady state, and $h_{a/s}$ and $h_{g/s}$, which determine the heat flow rate at the boundary, on B.

4. Samples

We selected a total of 19 CO_2-rich fluid inclusions hosted in mineral separates of five species; olivine, orthopyroxene, clinopyroxene, spinel, and colorless quartz (Fig. 2). Fluid inclusions in olivine, orthopyroxene, clinopyroxene, and spinel are derived from a mantle xenolith designated as "En2A" from Ennokentiev, Sikhote-Alin, Far Eastern Russia. Petrological descriptions were presented by Yamamoto et al. (2012). Quartz-hosted fluid inclusions are derived from pegmatites of Kadugannawa Complex from Owala-Kaikawala area, Matale, Sri Lanka. Seven mineral grains were selected and made into doubly polished chips. The fluid inclusion compositions are investigated using Raman spectroscopic analysis; volatile species other than CO_2 and H_2O are not detected. Although no H_2O liquid phase was visible under microscopic observation, trace amounts of H_2O were confirmed in Raman spectra from some

Table 1
Optical and thermal transfer properties of host mineral.

	α_h at 532 nm [a, b]	K_h at ~300 K [c, d]	k_h at ~300 K [c, d]	n_h [e]
	cm^{-1}	W/mK	mm^2/s	–
Olivine	1.14	5.50	2.05	1.65
Orthopyroxene	9.60	5.85	2.17	1.66
Clinopyroxene	3.07	6.21	2.40	1.65
Spinel	20.30	5.50	1.79	1.72
Quartz	0.02	9.00	5.19	1.55

[a] The compositions of each mineral are $Mg_{1.880}Fe_{0.106}Ca_{0.002}Mn_{0.006}Si_{1.002}O_4$, $(Mg_{1.63}Fe_{0.27}Ca_{0.04}Al_{0.02})Si_{1.97}Al_{0.03}O_6$, $(Ca_{0.948}, Fe_{0.056}, Na_{0.040})_{1.044}$ $(Ti_{0.003}, Mg_{0.941}, Cr_{0.024}, Al_{0.004})_{0.972}Si_{1.993}O_6$, $Mg_{1.01}Fe^{3+}{}_{0.01}Al_{1.99}Cr_{<0.01}O_4$, and quartz glass, respectively.

[b] α_h are compiled from Taran and Matsyuk (2013) for olivine, Taran and Langer (2001) for orthopyroxene, Taran et al. (2011) for clinopyroxene, Taran et al. (2014) for spinel, and Khashan and Nassif (2001) for quartz.

[c] The compositions of each mineral are Fo93, En89, Diopside, $Mg_{0.5}Fe_{0.5}AlO_4$, and SiO_2, respectively.

[d] K_h and k_h are compiled from Osako et al. (2004) for olivine, Hofmeister (2012) for orthopyroxene, Wang et al. (2014) for clinopyroxene, Hofmeister (2001) for spinel, and Branlund and Hofmeister (2007) for quartz.

[e] n_h are compiled from Lucey (1998) for olivine, orthopyroxene, and clinopyroxene, Palik (1998) for spinel, and Ghosh (1999) for quartz.

Table 2
List of parameters, their abbreviations and units.

Symbol	Parameter and unit
B	Laser heating coefficient [°C/mW]
B_{Raman}	Laser heating coefficient determined by hot band thermometer [°C/mW]
$h_{a/s}$	Heat transfer coefficient at air–sample boundary [W/m^{2}K]
$h_{g/s}$	Heat transfer coefficient at glass–sample boundary [W/m^{2}K]
H_h	Host mineral thickness [μm]
$\left(\frac{I^+_{HB}+I^-_{HB}}{I^+_{FD}+I^-_{FD}}\right)^{calc}$	Hot bands to the Fermi diad intensity ratio calculated by substituting density and temperature into Eq. (5) [−]
$\left(\frac{I^+_{HB}+I^-_{HB}}{I^+_{FD}+I^-_{FD}}\right)^{calib\ Eq.S1}$	Calibrated hot bands to the Fermi diad intensity ratio defined as $\left(\frac{I^+_{HB}+I^-_{HB}}{I^+_{FD}+I^-_{FD}}\right)^{sens.calib,ave}+\delta_{HB/FD}$ [−]
$\left(\frac{I^+_{HB}+I^-_{HB}}{I^+_{FD}+I^-_{FD}}\right)^{sens.calib,ave}$	Average of sensitivity calibrated hot bands to the Fermi diad intensity ratio at each measurement condition [−]
I_0	Laser intensity at the center of the beam-waist [W/m^2]
I_{ill}	Spatial distribution of the focused laser intensity [W/m^2]
K_h	Thermal conductivity of host mineral [W/mK]
k_h	Thermal diffusivity of host mineral [m^2/s]
K_{inc}	Thermal conductivity of inclusion [W/mK]
k_{inc}	Thermal diffusivity of inclusion [m^2/s]
L	Depth of an illuminated point [m]
n_a	Refractive index of air [−]
n_h	Refractive index of host mineral [−]
q	Radial distance from the optical axis of an illuminated point [m]
R_h	Equivalent circle radius of projected area of host mineral [μm]
r_{inc}	Equivalent circle radius of projected area of inclusion [μm]
T_{sample}	Initial temperature of the sample [°C]
$t_{N-2,\ 31.7\%}$	Two-tailed t-distribution at $N-2$ degrees of freedom (confidence level is 68.3%) [−]
$t_{0.9}$	Time required for temperature reaches 90% of its steady-state value [s]
T_h	Homogenization temperature [°C]
w_0	Waist-radius [μm]
$w(L, z_1)$	Beam waist radius at the axial position defined by Eq. (4) [μm]
z_0	Rayleigh range [μm]
z_1	Nominal focal position [μm]
z_{inc}	Inclusion depth from sample surface [μm]
α_h	Absorption coefficient of host mineral [cm^{-1}]
α_{inc}	Absorption coefficient of inclusion [cm^{-1}]
$\delta_{HB/FD}$	Correction term for hot bands to the Fermi diad intensity ratio [−]
δ_Δ	Correction term for Fermi diad splits [cm^{-1}]
$\Delta^{Ne\ calib}$	Distance of Fermi diad splits calibrated by using distances between the Ne lines [cm^{-1}]
$\Delta^{Ne\ \&\ Qtz\ calib}$	Distance of Fermi diad splits calibrated by using both Ne lines and a standard fluid inclusion in quartz [cm^{-1}]
Δ	Distance of Fermi diad splits [cm^{-1}]
λ	Wavelength of excitation laser [nm]
ρ	Density of a fluid inclusion [g/cm^3]
ρ_{Raman}	Density estimated from distance of Fermi diad splits [g/cm^3]
ρ_{Th}	Density estimated from homogenization temperature [g/cm^3]
σ_{BRaman}	Standard errors of laser heating coefficient determined by hot band thermometer [°C/mW]
σ_{Pill}	Uncertainty of the laser power defined as $\sigma_{Pill}=0.03\times P_{ill}$ [mW]

inclusions. Therefore, the composition of the fluid inclusions used for this study is approximately binary CO_2–H_2O. The CO_2 homogenization temperatures are measured using a heating–cooling stage (THMS600; Linkam Scientific Instruments Ltd.) at Hokkaido University. The instrument was calibrated using the melting points of H_2O (0.0 °C) in synthetic pure H_2O fluid inclusions. Homogenization were recorded at the heating rate of 0.1 °C/min. Fluid densities are calculated as described by Span and Wagner (1996), as shown in Table 3.

The respective sizes and depths of the fluid inclusions were measured using a 2000× objective (VH-ZST; Keyence Co.) with a digital microscope (VHX-5000; Keyence Co.). The projected area of fluid inclusions was measured automatically by identifying the outline of a fluid inclusion using the brightness contrast. The inclusion radius (r_{inc}) was defined by the equivalent circle radius of the obtained projected area. We also measured the equivalent circle radius of projected area of host mineral (R_h). We calculated the depth of the inclusion from the distance between the mechanical position for focus at the top of the host mineral and at a position where we obtained a sharp image of a fluid inclusion. The actual depth (z_{inc}) is calculated approximately by the simple expression of z_{inc} = refractive index of host mineral (n_h) × measured depth. As shown in Table 1, the values of n_h of olivine, orthopyroxene, clinopyroxene, spinel, and quartz are, respectively, 1.65, 1.66, 1.65, 1.72, and 1.55 (Lucey, 1998; Palik, 1998; Ghosh, 1999). In addition to z_{inc}, the host mineral thickness (H_h), which is defined by the distance between the mechanical position for focus at the surface of the host mineral and top of the slide glass, is shown in Table 3.

5. Experiment procedures

5.1. Overview of the hot band to Fermi diad intensity ratio thermometer

The CO_2 fluid temperature can be estimated using Raman spectra: a so-called hot band thermometer was developed using a high pressure optical cell (HPOC) (Rosso and Bodnar, 1995; Arakawa et al., 2008; Hagiwara et al., 2018). The experimental calibrations of earlier studies do not cover the P–T conditions of our interest. Therefore, we expanded the applicable P–T range using newly measured Raman spectra of CO_2 from 23 to 200 °C in approximately 20 °C increments under 10 temperature conditions (Fig. S1). Specific temperature, pressure, and density conditions are presented in Table S1. Details of the experimental apparatuses and procedures are provided in online Supplementary materials S1.

Fig. 3 shows the hot band to Fermi diad intensity ratio ($[I^+_{H.B.}+I^-_{H.B.}]/[I^+_{F.D.}+I^-_{F.D.}]$) versus the density of CO_2 fluid at temperatures of 23–200 °C. We proposed a new equation relating $[I^+_{H.B.}+I^-_{H.B.}]/[I^+_{F.D.}+I^-_{F.D.}]$, temperature ($T$; °C), and density ($\rho$; g/cm^3) as.

$$T = a + b\rho + c\rho^2 + d\rho^3 + e\left(\frac{I^+_{HB}+I^-_{HB}}{I^+_{FD}+I^-_{FD}}\right) + f\left(\frac{I^+_{HB}+I^-_{HB}}{I^+_{FD}+I^-_{FD}}\right)^2 + g\left(\frac{I^+_{HB}+I^-_{HB}}{I^+_{FD}+I^-_{FD}}\right)^3 + h\rho\left(\frac{I^+_{HB}+I^-_{HB}}{I^+_{FD}+I^-_{FD}}\right), \quad (5)$$

where a through h represent fitting parameters ($a=-472.925$, $b=1074.306$, $c=-985.102$, $d=325.905$, $e=3855.1$, $f=-17{,}374.6$, $g=44{,}140.7$, and $h=-385.88$). Also, Eq. (5) is useful at $0.6<\rho<1.2$ g/cm^3 and $23<T<200$ °C. The maximum absolute value of residual errors for all 131 measurements was 9.5 °C. The average of the absolute value of residual errors was 2.0 °C. Applicability of this thermometer for natural fluid inclusions was confirmed from natural fluid inclusions in quartz, which are shown as square (temperature increasing cycle) and triangle (decreasing cycle) symbols in Fig. 3. This test experiments were performed with a laser power of 7.7 mW because our experiments show that the hot band to Fermi diad intensity ratio of a CO_2 inclusion in quartz does not change for laser powers up to at least 15 mW (Fig. S2 and Table S2).

5.2. Raman setup

To determine B, Raman spectra of fluid inclusions were measured using P_{ill} ranging from 4.2 to 14.2 mW along both laser increasing and decreasing cycles. The values of P_{ill} during the experiments were measured using a laser power meter (PD300-ROHS; Ophir Optronics Ltd.). The uncertainty of the measured P_{ill} is ±3%. During the measurement, T_{sample} was controlled by the room temperature, which was controlled by an air conditioner. The sample was placed on the Linkam stage. The actual T_{sample} was monitored by the thermocouple of the

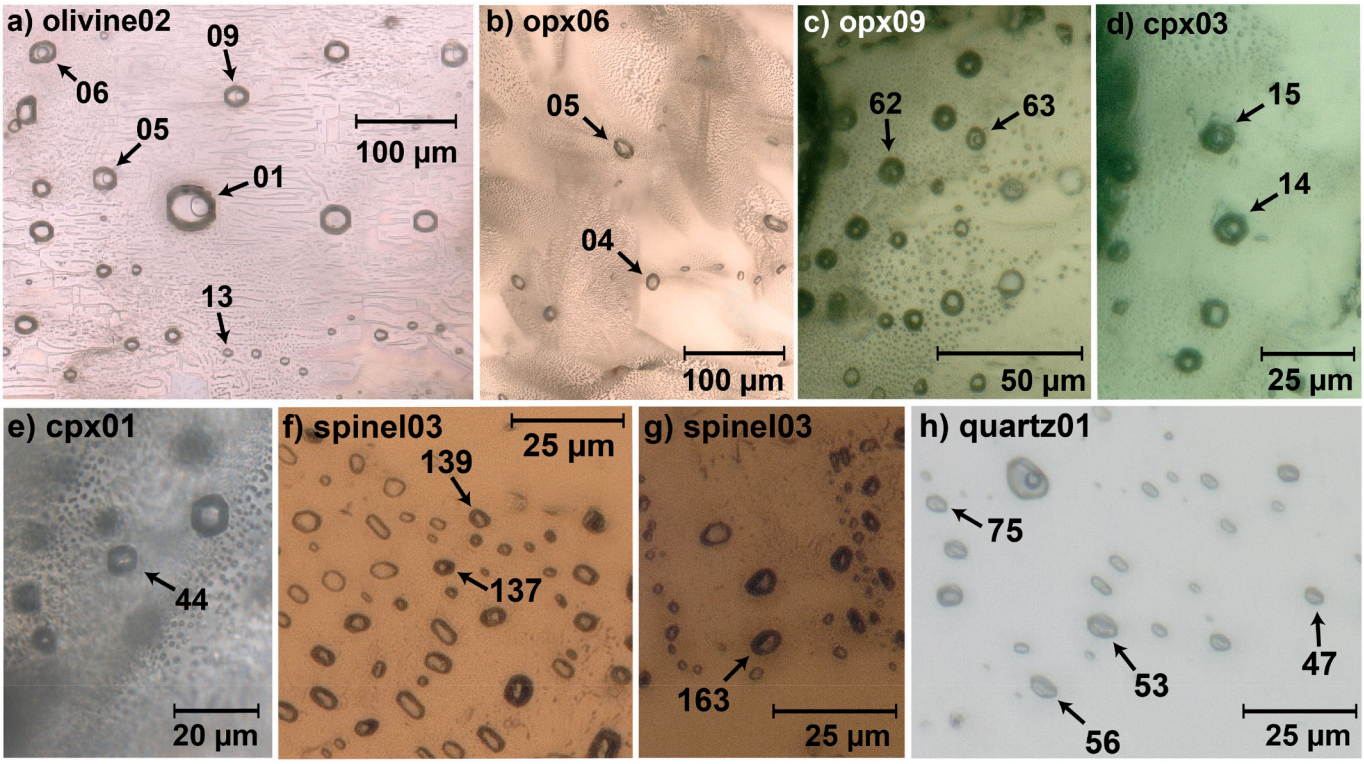

Fig. 2. Photomicrographs of studied fluid inclusions hosted in olivine (a), orthopyroxene (b and c), clinopyroxene (d and e), spinel (f and g), and quartz (h) in transmitted light. A total of 19 fluid inclusions are selected for determination of laser heating coefficient. To increase the depth of field in their photomicrographs, multi-focus ("stacking") techniques were applied except for Fig. 2e.

Table 3
Microthermometric data and geometric properties of fluid inclusions and host minerals.

	T_h[a] °C	ρ_{Th} g/cm^3	r_{inc} μm	z_{inc} μm	H_h μm	R_h μm
En2A oli02 fi01	26.4	0.687	22.2	75.4	497	1548
En2A oli02 fi05	26.7	0.682	11.2	47.5	497	1548
En2A oli02 fi06	26.2	0.691	11.5	59.9	497	1548
En2A oli02 fi09	25.6	0.701	10.9	96.4	497	1548
En2A oli02 fi13	25.8	0.698	4.5	42.9	497	1548
En2A opx06 fi04	26.2	0.691	7.4	73.7	461	1191
En2A opx06 fi05	25.6	0.701	9.3	50.5	461	1191
En2A opx09 fi62	26.4	0.687	4.8	12.5	270	1084
En2A opx09 fi63	26.4	0.687	3.7	7.0	270	1084
En2A cpx03 fi14	27.0	0.676	4.6	2.6	252	841
En2A cpx03 fi15	26.9	0.678	4.5	3.3	252	841
En2A cpx01 fi44	25.2	0.707	3.4	25.5	189	807
En2A sp03 fi137	26.1	0.693	2.0	8.6	42	534
En2A sp03 fi139	25.6	0.701	2.0	2.6	42	534
En2A sp03 fi163	26.0	0.694	2.8	5.7	42	534
Quartz 01 fi 47	19.6	0.778	2.0	8.2	743	5645
Quartz 01 fi 53	18.8	0.786	2.9	14.6	743	5645
Quartz 01 fi 56	18.8	0.786	2.6	4.5	743	5645
Quartz 01 fi 75	18.7	0.787	2.0	44.8	743	5645

[a] Temperature of partial homogenization of the carbonic phase to liquid.

Linkam stage. In this study, measurements are performed without a silver lid so that the sample and the ambient air can quickly reach thermal equilibrium. Measurements were performed five times at each P_{ill}. Measured $[I^+_{H.B.} + I^-_{H.B.}]/[I^+_{F.D.} + I^-_{F.D.}]$ were converted to temperature using Eq. (5). Table S3 presents the T_{sample} and average fluid temperatures of five measurements and their standard deviation (1σ) at each P_{ill}. Note that, T_{sample} of quartz is not reported in Table S3 (see the paragraphs below for details). The duration of every Raman analysis is 300 or 600 s.

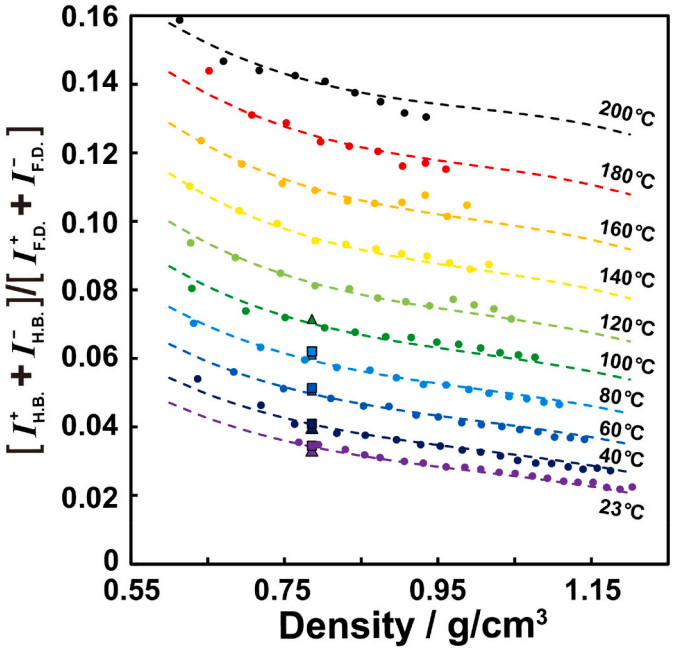

Fig. 3. Effects of density and temperature on the hot band to the Fermi diad intensity ratio of CO_2. Circles represent data obtained from high-pressure optical cell experiments and data are presented in Table S1. The dashed lines represent the best fit to data. The calibrated hot band to Fermi diad intensity ratio (i.e., $[I^+_{H.B.} + I^-_{H.B.}]/[I^+_{F.D.} + I^-_{F.D.}]^{sens.\ calib} + \delta_{HB/FD}$) and density obtained from a natural fluid inclusion at 26, 40, 60, 80, and 100 °C are plotted as square and triangle symbols, which are measured respectively along the temperature increasing and decreasing cycle (Table S4). $\delta_{HB/FD}$ was calculated as −0.0075 (Table S4).

Raman spectra of the CO_2 fluid were obtained using a micro-Raman spectrum analysis system set up at the Hokkaido University Museum, with 1200 grooves/mm grating. Raman spectra were acquired using diode-pumped solid-state laser (532 nm, Gem 532; Laser Quantum) excitation, a spectrometer with 75 cm focal length (Acton SP-2750; Princeton Instruments, Inc.), and a CCD camera (1650 × 200 pixels, 16-μm width, iVac; Andor Technology). A Nikon microscope (ECLIPSE E600-POL) with a × 50 (N.A. = 0.8, LU Plan; Nikon Corp.) objective was used to focus on the samples. Spectra were collected in a single window between 656 and 1481 cm^{-1}.

In the case of fluid inclusions in quartz, which requires higher P_{ill} for accurate determination of B, almost identical measurements were performed using a micro-Raman spectrum analysis system (RAMANtouch VIS-HP-MAST; Nanophoton) at JAMSTEC. The laser output was 1500–4000 mW at the source. Using neutral-density filters with variable transmission, we adjusted P_{ill} at the sample surface from 5 to 351 mW. Raman spectra were acquired using semiconductor laser (532 nm) excitation, a 1200 grooves/mm grating, and a CCD camera (1340 × 400 pixels). In this experiment, the sample was placed on a slide glass, not on a Linkam stage. Therefore, T_{sample} is not measured directly. The ambient temperature during the measurement was monitored using a thermometer (TR-73 U; T&D Corp.) placed next to a microscope and was almost constant at the range of 20.2–22.1 °C. A Nikon objective (N.A. = 0.8, TU Plan ×50) was used to focus on the samples. The duration of every Raman analysis is 30 to 300 s. Spectra were collected in a single window between 559 and 1780 cm^{-1}. Sensitivity calibration, spectra fitting, and data correction procedures are described in Supplementary material S1 and Tables S4 and S5. The average of the sensitivity calibrated hot band to Fermi diad intensity ratio at each P_{ill} ($[I^{+}_{H.B.} + I^{-}_{H.B.}]/[I^{+}_{F.D.} + I^{-}_{F.D.}]^{sens.\ calib,\ avg}$) is presented in Table S3.

5.3. Specific procedures for laser heating coefficient determination and error analysis

Earlier reports have described linear correlation between sample temperature and P_{ill} (Kagi et al., 1994; Liu et al., 1995; Haro-González et al., 2013; Català et al., 2017). Therefore, we can also expect the linear increase of inclusion temperature with P_{ill}. Fig. 4 presents relations between P_{ill} and the inclusion temperature obtained from simulations. Actual data obtained from spinel03 fi139 are also presented as an example. The open symbols show the simulated relation between P_{ill} and inclusion temperature calculated using finite element method. Parameters used for the simulation are almost identical to the actual experimental conditions and listed in the caption of Fig. 4. The boundary conditions are calculated with varying $h_{g/s}$ from 5 to 50 W/m^2K. As all measured results show the linear relation between inclusion temperature and P_{ill} (Fig. 4 for an example), we define B as the slope of the linear fit of the measured values. The red and blue circles respectively present the measured data obtained from laser increasing and decreasing cycles. For estimating the best fit straight line to data, we applied bivariate least squares fitting method (York method) using OriginPro9.0 (solid line in Fig. 4). In this case, we obtained the slopes (B_{Raman}) and those of errors as 6.1 ± 0.6 °C/mW. To construct 68.3% confidence intervals around the calculated slopes, we used the two-tailed t-distribution at $N - 2$ degrees of freedom ($t_{N-2,\ 31.7\%}$) and the standard errors of the slopes (σ_{BRaman}). Estimated slopes and those of 68.3% confidence intervals ($\sigma_{BRaman} \times t_{N-2,\ 31.7\%}$) are presented in Table 4.

6. Results

6.1. Finite element method

6.1.1. Simulation of temperature distribution inside the host mineral

In Fig. 5, we present a typical q–z section of the stationary temperature distribution around the inclusion (parameters are those of spinel03 fi139). We set $h_{g/s}$ as 10 W/m^2K. Similarly to earlier studies, the radial temperature distribution from the optical axis at the laser focus showed logarithmic distance dependence (upper inset of Fig. 5) (Celliers and

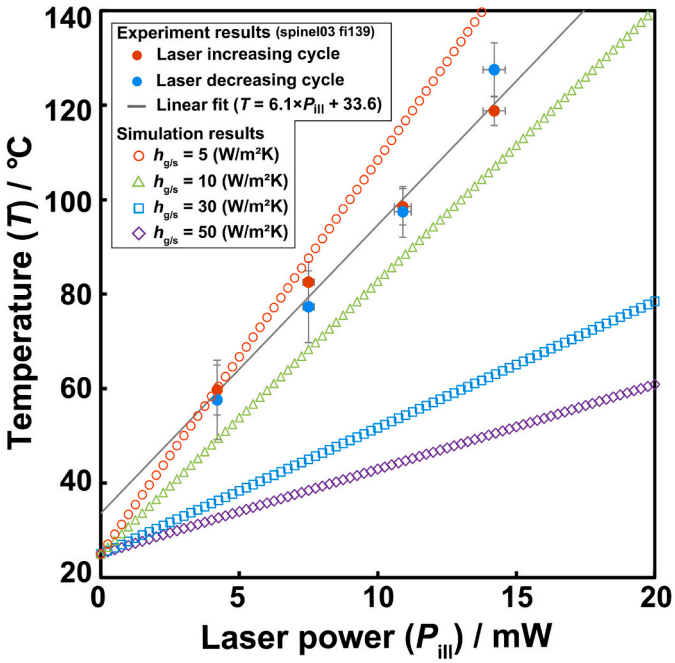

Fig. 4. Measured and simulated inclusion temperature as a function of laser power. Red and blue filled circles represent the data obtained from the fluid inclusion in spinel (spinel03 fi139) and measured respectively along the laser increasing and decreasing cycles. Error bars for temperature show the standard deviation (n = 5). Those for laser power are 3%. These data are presented in Table S3. A solid line shows the linear fit (York method) to eight data points. The laser heating coefficient determined from the linear fit is 6.1 ± 0.6 °C/mW. Open symbols show the simulated relations between inclusion temperature and laser power. Parameters used for simulation are the following: T_{sample} = 25 °C, λ = 532 nm, P_{ill} = 0–20 mW, w_0 = 1.46 μm, α_{inc} = 0 m^{-1}, z_{inc} = 2.6 μm, r_{inc} = 2.0 μm, K_{inc} = 0.08 W/mK, k_{inc} = 0.02 mm^2/s, H_h = 42 μm, R_h = 0.534 mm, K_h = 5.5 W/mK, k_h = 1.79 mm^2/s, α_h = 2030 m^{-1}, n_h = 1.72, $h_{a/s}$ = 5 W/m^2K, and $h_{g/s}$ = 5–50 W/m^2K. (For interpretation of the references to colour in this figure legend, the reader is referred to the web version of this article.)

Table 4
Laser heating coefficients and errors obtained from natural fluid inclusions by using hot band thermometer.

Sample	B_{Raman}	$\sigma_{BRaman} \times t_{N-2,\ 31.7\%}$
	°C/mW	°C/mW
En2A oli02 fi01	1.0	0.3
En2A oli02 fi05	0.5	0.4
En2A oli02 fi06	0.02	0.2
En2A oli02 fi09	0.4	0.4
En2A oli02 fi13	0.6	0.3
En2A opx06 fi04	0.8	0.3
En2A opx06 fi05	0.5	0.2
En2A opx09 fi62	1.2	0.2
En2A opx09 fi63	0.7	0.3
En2A cpx03 fi14	0.6	0.2
En2A cpx03 fi15	0.7	0.2
En2A cpx01 fi44	1.3	1.4
En2A sp03 fi137	5.2	0.9
En2A sp03 fi139	6.1	0.6
En2A sp03 fi163	6.4	1.1
Quartz 01 fi 47	0.014	0.002
Quartz 01 fi 53	0.012	0.001
Quartz 01 fi 56	0.010	0.002
Quartz 01 fi 75	0.013	0.002

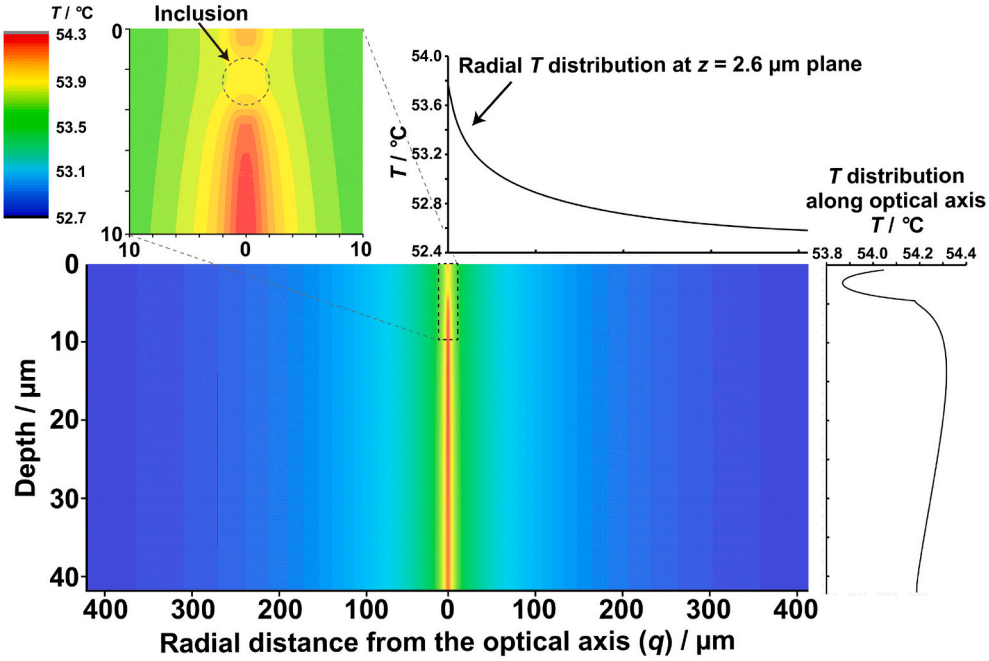

Fig. 5. Simulation of stationary temperature distribution inside the host mineral containing inclusion at z_{inc} = 2.6 μm. Radial temperature distributions at the z_{inc} = 2.6 μm plane following the ln(1/q) decay (upper inset graph). The temperature along the optical axis becomes minimum at z = 2.3 μm (right inset graph). The inset schematic shown at upper left is an enlarged view of the temperature distribution around and within a fluid inclusion. Parameters used for simulations are the following: T_{sample} = 25 °C, λ = 532 nm, P_{ill} = 5 mW, w_0 = 1.46 μm, α_{inc} = 0 m^{-1}, z_{inc} = 2.6 μm, r_{inc} = 2.0 μm, K_{inc} = 0.08 W/mK, k_{inc} = 0.02 mm^2/s, H_h = 42 μm, R_h = 0.534 mm, K_h = 5.5 W/mK, k_h = 1.79 mm^2/s, α_h = 2030 m^{-1}, n_h = 1.72, $h_{a/s}$ = 5 W/m^{2}K, and $h_{g/s}$ = 10 W/m^{2}K. It is noteworthy that, although simulations were performed assuming R_h = 0.534 mm, this schematic depicts the radial distance up to around 0.42 mm because the isotherm farthest from the optical axis existed at around q = 0.42 mm.

Conia, 2000; Mao et al., 2005; Haro-González et al., 2013; Català et al., 2017). In addition, reports of earlier studies described that the temperature distribution along the optical axis also shows logarithmic decay (Català et al., 2017). However, our simulation results do not follow such a monotonic decrease (right inset of Fig. 5). Compared to results of earlier studies, our simulated temperature distributions along the optical axis show complex behavior: temperatures take a minimum value at $z \sim z_{inc}$; the temperature decreases gradually after taking a maximum value at $z > z_{inc}$.

6.1.2. *Laser heating coefficient as functions of experimental, geometrical, and optical variables*

In Fig. 6, we present simulation of the effect of each variable on B by changing each parameter within the range that can occur in the study of inclusions. The parameters used in the simulation are presented in the caption in Fig. 6.

Our simulation results showed a linear relation between B and α_h (Fig. 6a). Although B and H_h have a positive relation throughout whole simulated H_h, it almost reaches a plateau when H_h was greater than 200 μm (Fig. 6b). For H_h < 100 μm, B decreases rapidly as H_h decreases (Fig. 6b). Although R_h and B show negative correlation, B remains nearly constant even as R_h increases when R_h exceeds 4 mm (Fig. 6c). The negative correlation between B and K_h was confirmed by our simulations (Fig. 6d). k_h and n_h did not influence B (Fig. 6e and f). We investigated the r_{inc} dependence of B over r_{inc} = 0.1–10 μm at z_{inc} = 10 μm, which revealed that B decreases slightly, concomitantly with increasing r_{inc} (inset in Fig. 6g). Additionally, we simulated the size dependence of B at z_{inc} = 100 μm from r_{inc} = 0.1–50 μm. As a result, the relation between B and r_{inc} was completely the same as that at z_{inc} = 10 μm when $r_{inc} \leq$ 10 μm, but the amount of change increased dramatically at r_{inc} > 10 μm (inset in Fig. 6g). Our simulation results show an exponential decrease (i.e., $B \propto \exp.(-r_{inc})$), whereas those of Català et al. (2017) show logarithmic decay (i.e., $B \propto -\log(r_{inc})$). By contrast, in the case of $\alpha_{inc} > \alpha_h$, B clearly increases concomitantly with increasing r_{inc} at constant w_0 (Figs. 6i and 7), probably because the inclusions generate heat more efficiently than the host minerals when $\alpha_{inc} > \alpha_h$. We investigated z_{inc} dependence of B. It decreases near both the air–sample and glass–sample boundaries. However, the variation of B was very slight (Fig. 6h). We investigated variations of B by changing α_{inc} from 10^{-4} to 10^2 cm^{-1} and r_{inc} from 0.1 to 2.5 μm while maintaining α_h = 1.14 cm^{-1} (Fig. 6i). As a result, the effect of α_{inc} on B is negligible when α_{inc} < approx. 0.1–1 cm^{-1}, but it cannot be negligible when α_{inc} > approx. 0.1–1 cm^{-1}. The transition of the effect of α_{inc} on B occurs around α_{inc} = 1 cm^{-1}, which is comparable to α_h (1.14 cm^{-1}). Therefore, the impact of α_{inc} on B cannot be negligible when $\alpha_{inc} > \alpha_h$ (Fig. 6i). Fig. 6j presents evaluation of the effect of λ dependence of Rayleigh length on B, assuming constant α_h (= 1.14 cm^{-1}). As a result, the difference in λ did not affect B between 300 and 1100 nm. Negative correlation between B and w_0 was observed when α_{inc} is 100 and 1 cm^{-1} (Fig. 6k). However, B was constant when α_{inc} is 0 and 0.01 cm^{-1}, irrespective of w_0. If $\alpha_{inc} < \alpha_h$ and if r_{inc} is constant (each solid line in Fig. 7), then B is constant because heat generation is ineffective at the focus, which has the highest energy density and the highest potential for heat generation. The larger $h_{a/s}$ (or $h_{g/s}$) becomes, the smaller B is (Fig. 6l and Fig. S3).

Among the parameters used for the simulations, α_h, H_h, R_h, α_{inc}, $h_{a/s}$, and $h_{g/s}$ strongly affected B. In fact, B changed about one order of magnitude or more in the investigated range. However, k_h, n_h, z_{inc}, and λ do not affect B. In addition, K_h, r_{inc}, and w_0 slightly affect B.

6.1.3. *Temporal evolution of temperature distribution*

We simulated the temporal evolution of the inclusion temperature when the inclusions were irradiated with 0.5, 5, and 50 mW excitation laser, and found that the inclusion temperature approached the steady-state value asymptotically with time (Fig. 8). Simulations were performed by assuming geometrical and material parameters the same as those of spinel03 fi139. Details of parameters are described in the caption of Fig. 8. As a result, $t_{0.9}$ (= time required for temperature reaches 90% of its steady-state value) was reached in about 18.5 s. Furthermore, varying P_{ill} from 0.5 to 50 mW does not affect $t_{0.9}$ (Fig. S4j). Therefore, even if we analyze the same inclusion with different P_{ill}, the difference does not affect the time required for the system to reach its steady state. However, according to simulation of Català et al. (2017), the temperature of microbeads in water reaches 90% of its steady state value only after 1 ms, which is four orders of magnitude lower than our results. To clarify the causes of such differences in $t_{0.9}$, we investigated the effects of experimental parameters on $t_{0.9}$ (Fig. S4). Additionally, we simulated $t_{0.9}$ as functions of these parameters under four boundary conditions: $h_{g/s}$ = 0, 10, 1000 W/m^{2}K, and Dirichlet boundary condition (Fig. S5). As a result, the only parameters that can change $t_{0.9}$ as many as 4 orders of magnitude was the

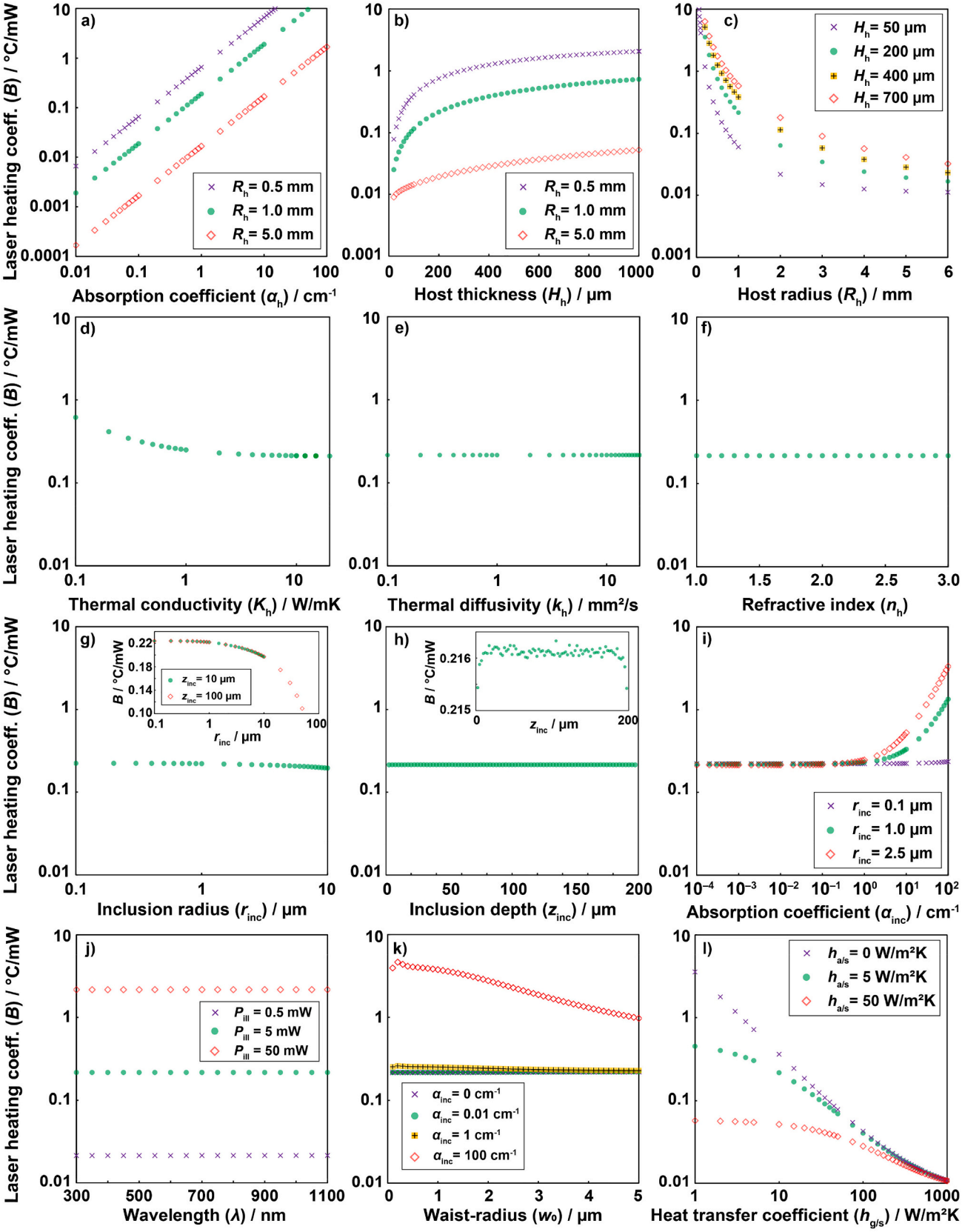

Fig. 6. Simulated laser heating coefficient as functions of a–f) host mineral, g–i) inclusion, and j–l) experimental parameters. Parameters used for simulations are fundamentally the following otherwise used as variables in each figure: $T_{sample} = 25$ °C, $\lambda = 532$ nm, $P_{ill} = 5$ mW, $w_0 = 1.46$ μm, $\alpha_{inc} = 0$ m^{-1}, $z_{inc} = 10$ μm, $r_{inc} = 2.5$ μm, $K_{inc} = 0.08$ W/mK, $k_{inc} = 0.02$ mm^2/s, $H_h = 200$ μm, $R_h = 1$ mm, $K_h = 5.5$ W/mK, $k_h = 2.05$ mm^2/s, $\alpha_h = 114$ m^{-1}, $n_h = 1.65$, $h_{a/s} = 5$ W/m^{2}K, and $h_{g/s} = 10$ W/m^{2}K.

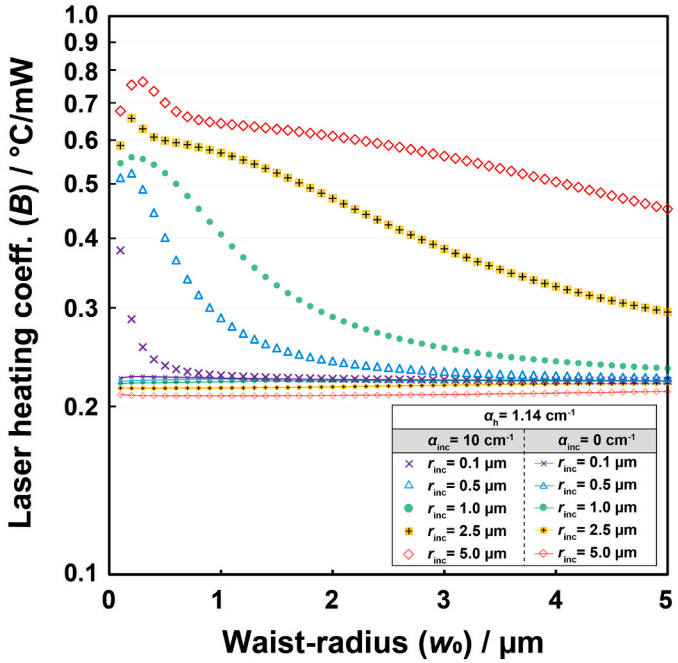

Fig. 7. Simulated laser heating coefficient as a function of waist-radius (w_0), inclusion radius (r_{inc}), and absorption coefficient of the inclusion (α_{inc}). When α_{inc} is 0 cm^{-1}, the laser heating coefficient is constant independent of the w_0, but the laser heating coefficient becomes smaller with increasing r_{inc}. However, when α_{inc} is 10 cm^{-1}, the laser heating coefficient increases with decreasing w_0. When α_{inc} = 10 cm^{-1}, the r_{inc} is larger with a larger laser heating coefficient. The following parameters are used for simulations: T_{sample} = 25 °C, λ = 532 nm, P_{ill} = 5 mW, w_0 = 0.1–5.0 μm, α_{inc} = 0 and 1000 m^{-1}, z_{inc} = 10 μm, r_{inc} = 0.1–5.0 μm, K_{inc} = 0.08 W/mK, k_{inc} = 0.02 mm^2/s, H_h = 200 μm, R_h = 1 mm, K_h = 5.5 W/mK, k_h = 2.05 mm^2/s, α_h = 114 m^{-1}, n_h = 1.65, $h_{a/s}$ = 5 W/m^2K, and $h_{g/s}$ = 10 W/m^2K.

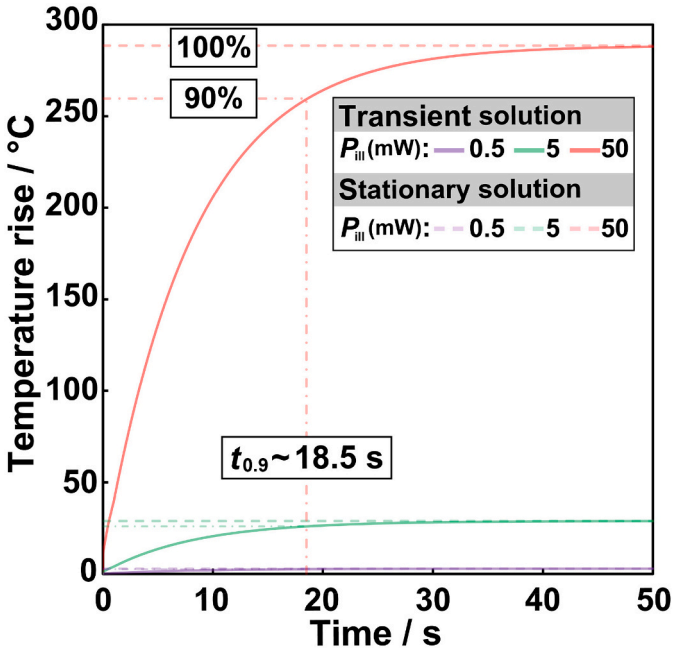

Fig. 8. Temporal evolution of the temperature rise of inclusions when irradiated with a 0.5, 5, or 50 mW laser. Optical and geometrical parameters of the host mineral and inclusion used for calculation are spinel and spinel03 fi139, respectively, as listed in Tables 1 and 3. With time, it approaches the temperature rise of the steady-state solution shown by the dotted horizontal line. Horizontal dashed–dotted lines show the temperature rise of 90% of its steady-state value. $t_{0.9}$ represents the time at which the temperature reaches 90% of its steady-state value. Parameters used for simulations are the following: T_{sample} = 25 °C, λ = 532 nm, P_{ill} = 0.5–50 mW, w_0 = 1.46 μm, α_{inc} = 0 m^{-1}, z_{inc} = 2.6 μm, r_{inc} = 2.0 μm, K_{inc} = 0.08 W/mK, k_{inc} = 0.02 mm^2/s, H_h = 42 μm, R_h = 0.534 mm, K_h = 5.5 W/mK, k_h = 1.79 mm^2/s, α_h = 2030 m^{-1}, n_h = 1.72, $h_{a/s}$ = 5 W/m^2K, and $h_{g/s}$ = 10 W/m^2K.

boundary condition. Therefore, because Català et al. (2017) set the boundary condition to the Dirichlet condition, the extremely small $t_{0.9}$ in their simulations will be attributable to the assumption of high heat flux at the boundary.

6.2. Experiments

The total of 19 laser heating coefficients obtained from Raman spectroscopy are presented in Fig. 9 as functions of host mineral and inclusion parameters.

Our experimentally obtained results show linear correlation between α_h and B (Fig. 9a). The mean B were quartz << olivine < opx ≈ cpx < < spinel (Fig. 9a and Table 4). Additionally, we found negative correlations between B and each of H_h, R_h, and K_h (Fig. 9b to d). However, these correlations are not necessarily causal because they might be apparent relations caused by parameters that are highly influential to B (see section 7.1 for details). In our experiments, we measured B_{Raman} of fluid inclusions in olivine with a radius of 4.5–22.2 μm, but no remarkable r_{inc} dependence of B was observed (Fig. 9e). From our simulations, B at r_{inc} = 4.5 μm was only 1.2 times larger than B at r_{inc} = 22.2 μm. Therefore, at least for r_{inc} < 22 μm, we conclude from both the experimental and simulation results that r_{inc} has little impact on B. Our experimentally obtained results show no systematic relation between z_{inc} and B (Fig. 9f). For example, B_{Raman} of the shallowest fluid inclusions for each host mineral species is identical to those of the deepest one, within the error (Fig. 9f).

7. Discussion

7.1. Influential variables on the laser heating of inclusions

Mao et al. (2005) proposed a laser heating model that describes a temperature profile in the focal plane at the middle of the chamber and parallel to the coverslips. Based on the model, Haro-González et al. (2013) presented the following relation at radial distance w_0 (=0.6λ/NA) from the optical axis of focus as

$$B = \frac{\alpha_h}{2\pi K_h} \times ln\left[\frac{H_h \times NA}{0.6\lambda}\right], \quad (6)$$

where K_h denotes the thermal conductivity, H_h represents the sample thickness, NA stands for the numerical aperture of an objective, and λ shows the laser wavelength.

Although earlier studies have argued that B is proportional to α_h/K_h (e.g., Català et al., 2017), we found that such conditions are limited to those in which the boundary condition is a Dirichlet condition. Also, the effect of K_h on B decreases as the heat transport at the interface decreases (Fig. S3d). The host minerals used for this study have K_h of 5.5–9.0 W/mK. Therefore, the expected difference in B is only about twice as large at most. Therefore, K_h is not the dominant factor in determining B, at least for the host minerals used for this study. However, if a large difference exists in K_h between materials (e.g., diamond and barite), then such K_h differences cause differences in B.

As one might infer from Eq. (6), the logarithmic relation between H_h and B is also confirmed by our simulation (Fig. 6b). To verify the effect of H_h on B from experimental data, we should compare the B of fluid inclusions in the same host mineral species with different thicknesses.

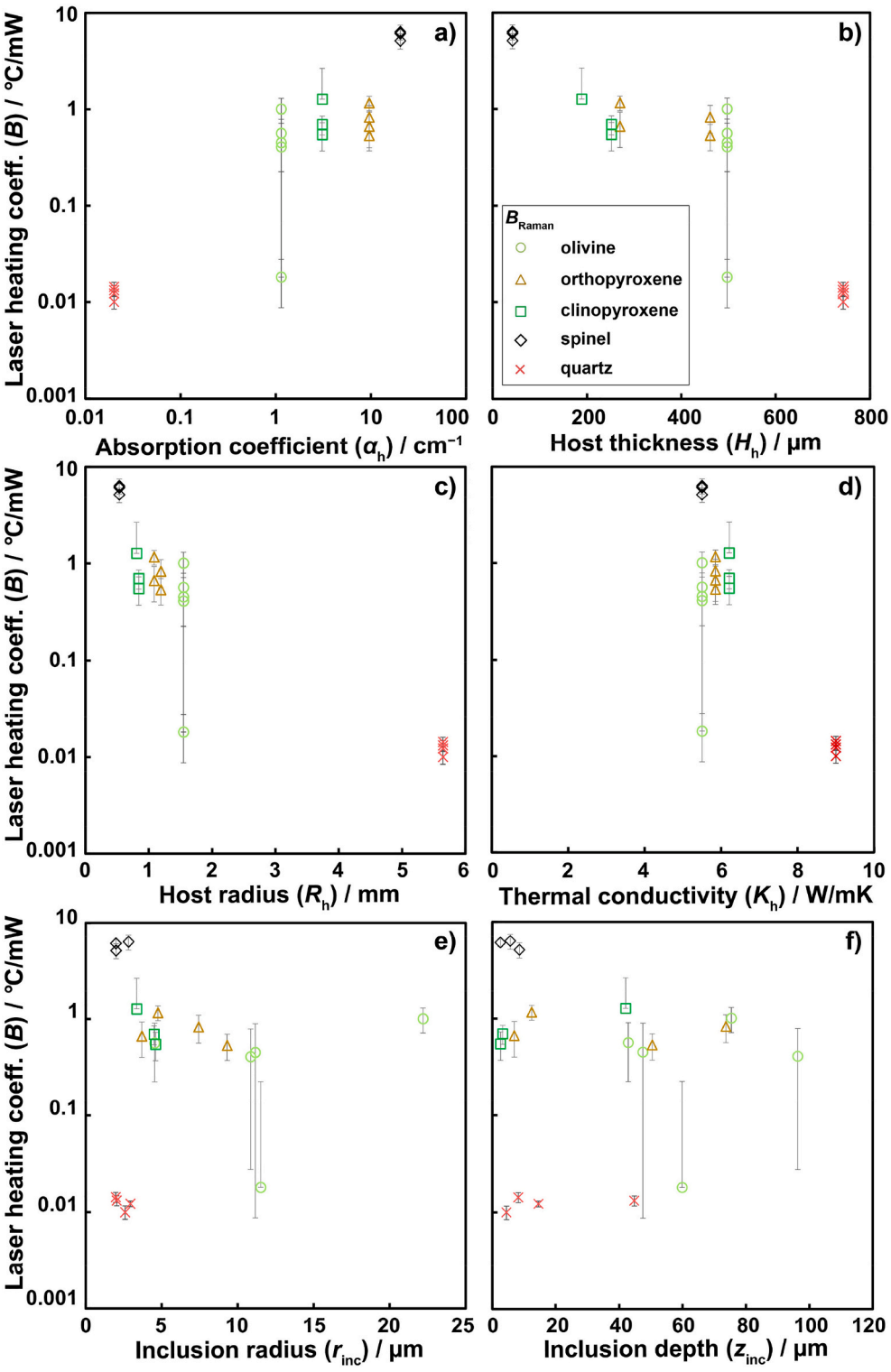

Fig. 9. Relations between material parameters and the laser heating coefficient of fluid inclusions measured by hot band thermometer: a) absorption coefficient of the host mineral, b) host mineral thickness, c) circle equivalent radius of the host mineral, d) thermal conductivity of the host mineral, e) radius of the fluid inclusion, and f) the distance of the fluid inclusion from the sample surface. Each graph shows a total of 19 data obtained using a hot band thermometer (B_{Raman}). Sample geometry, absorption coefficient, thermal conductivity, and laser heating coefficient are presented in Tables 1, 3, and 4.

Therefore, we use two orthopyroxene grains (opx06 and opx09) having almost identical R_h, but different H_h (461 and 270 μm, respectively) for comparison. As a result, no significant difference of measured B was found between them (Fig. 9b). This lack of difference is reasonable because our simulations show B as almost independent of H_h when $H_h >$ 200 μm. That result constitutes evidence that the effect of H_h on B is low compared with those of α_h within the parameter range that might occur in the inclusion study. Nevertheless, because B decreases rapidly as H_h decreases when $H_h < 100$ μm, the thinner sample better suppresses laser heating and thermal damage (Fig. 6b and Fig. S3b).

From the discussion presented above, the effects of H_h and K_h on B are small. From our simulations, the λ and w_0 effects on B are negligible, at least when $\alpha_{inc} < \alpha_h$ (Fig. 6j and k). Therefore, as expected from Eq. (6) and earlier studies, the dominant factor which determines B will be α_h (Català et al., 2017). Indeed, our simulation and experimentally obtained results showed a linear relation between them (Figs. 6a, 9a, and Fig. S3a). The spinel has about 10^3 times larger α_h than that of quartz: the measured B_{Raman} of spinel is approx. 6 °C/mW, which is 600 times

larger than that of quartz (approx. 0.01 °C/mW). In addition, B of orthopyroxene, clinopyroxene, and olivine, which have an intermediate α_h, fall between approx. 0.1 and 1 °C/mW, which lies between those of spinel and quartz. This order is equal to the order of α_h except for the order of clinopyroxene and orthopyroxene. Therefore, although it remains possible that parameters other than α_h affect B to some extent, our experiments and simulations support that the experimental parameter with the most influence on the B would be α_h, within the parameter range that could occur in the inclusion study, as suggested by results of earlier studies (Haro-González et al., 2013; Català et al., 2017).

According to Català et al. (2017), the boundary distance from the optical axis has little effect on B at least boundary distance >80 μm (i.e., R_h > 80 μm). However, unlike their results, our simulation results showed negative correlation between R_h and B (Fig. 6c and Fig. S3c). This discrepancy is expected to result from the difference in boundary conditions because Català et al. (2017) assumed a Dirichlet boundary condition, whereas we assumed a convective heat flux. In fact, when the glass–sample boundary condition is changed to the Dirichlet boundary condition in our simulation, R_h at which the relation between R_h and B reaches a plateau decreases drastically from approx. R_h = 4 mm to 0.2 mm (red circles in Fig. S3c). Therefore, the discrepancy of the simulation result is explainable by the difference of boundary conditions. To evaluate the effect of R_h on B from the experimental data, we need host minerals with different R_h. However, we have not prepared such samples in this study. Therefore, the effect of R_h on B cannot be discussed further from our experimental data. Nonetheless, earlier reports describe that even quartz, which has very small α_h, is heated to a considerable degree by a laser when R_h is small (Chio et al., 2003). Therefore, it would be effective NOT to make the host mineral too small during sample preparation to reduce the damage and spectral changes caused by the excitation laser.

Regarding the effects of r_{inc} on B, Peterman et al. (2003) concluded that only a small effect derives from the size of the trapped beads. By contrast, Català et al. (2017) concluded that B logarithmically decreases concomitantly with increasing bead size. It is related directly to the radial temperature profile. However, their data cannot be compared directly to those of the present study because both their experimental and simulation results have been based on the temperature of the buffer (either water or glycerol) rather than in the beads. Both our experimental and simulation results, which evaluated B of the inclusion itself, reveal that r_{inc} has little impact on B, when the inclusion radius is smaller than 22 μm. By contrast, our simulations indicate that the extremely large inclusion (r_{inc} > ~30 μm) shows B decrease concomitantly with increasing size (r_{inc}) because the temperature rise from the focused laser is restricted near the focal point (inset in Figs. 5 and 6g). Such a restriction of the temperature rise region has also been reported by Català et al. (2017). When we assume the case with $\alpha_{inc} > \alpha_h$, possible case for solid inclusions, the larger inclusions are more likely to be heated. The effect of laser heating must be considered when comparing results obtained from inclusions with highly different size (Fig. 7).

The experiments reported by Català et al. (2017) demonstrated that heating was decreased significantly when the laser was focused on a particle in water and placed 10 μm from the bottom of glass–water boundary; whereas B remained almost constant irrespective of depth in the case where the laser focus was distant from the bottom by >10 μm. They argued that the temperature rise from the focused laser around the focal point was restricted, with volume as small as 10 μm. Therefore, when the focus is close to the glass with a lower α/K, the heat produced by the laser is dissipated efficiently to the glass. In contrast, our simulation results show the B dependence on z_{inc} only when the glass–sample boundary condition was in a Dirichlet condition (Fig. S3h). Even in such a condition, B is almost constant near the $z = 0$ plane. Furthermore, the experimentally obtained results showed no z_{inc} dependence of B. Raman spectroscopy is usually applied to shallow inclusions rather than the bottom of the sample because the increase in inclusion depth generally makes it difficult to obtain the Raman scattered light of the inclusions efficiently (e.g., Everall, 2010). Therefore, z_{inc} dependence of B is negligible in a normal analysis environment. For that reason, no bias is found in measurements of inclusions with various depths. However, it is noteworthy that the proximity of inclusion to the thin-section surface might modify the residual pressure of inclusions (Mazzucchelli et al., 2018; Zhong et al., 2020).

Català et al. (2017) and Peterman et al. (2003) asserted that heating is governed mainly by laser absorption in the surrounding buffer, but not in the particles. In earlier studies, absorption coefficients of beads at their excitation wavelength were 0.06 cm^{-1} (polystyrene) and 5×10^{-5} cm^{-1}(silica), which were sufficiently lower than those of the surrounding buffer: water (0.14 cm^{-1}) and glycerol (0.21 cm^{-1}). Their results are consistent with our simulation results, which suggest that α_{inc} did not affect B when α_{inc} was lower than α_h. Here we consider two typical fluid species, CO_2 and H_2O, as examples. In the case of CO_2, α_{inc} at 532 nm is expected to be much smaller than that of quartz, which has the smallest α_h used for this study. Therefore, it is reasonable to assume $\alpha_{inc} = 0$ for the evaluation of laser heating in inclusions from Fig. 6i. Similarly, α_{inc} of pure water at 532 nm is approx. 2×10^{-4} cm^{-1}. Its temperature and salinity dependence are negligible; the assumption of $\alpha_{inc} = 0$ is also valid for brine fluid inclusions (Pegau et al., 1997; Röttgers et al., 2014). Conversely, the impact of α_{inc} cannot be negligible when $\alpha_{inc} > \alpha_h$ (Fig. 6i). For that case, B is controlled strongly by r_{inc}, α_{inc}, and w_0 (Figs. 6i and 7). Therefore, for $\alpha_{inc} > \alpha_h$, bias attributable to laser heating can occur when measuring inclusions of different r_{inc} and α_{inc} or with different objective lenses.

In summary, α_h, R_h, and $h_{g/s}$ have significant effects on B, but r_{inc} and z_{inc} do not affect B. Therefore, to reduce the temperature rise during the analysis of inclusions, it is effective to make the host mineral larger and thinner and to increase the heat flow rate at the boundary. In addition, α_h depends on the wavelength. Therefore, if the optimal excitation laser setting and sample geometry are selected, then the inclusion temperature during the analysis will be suppressed; the obtained data will approach the true value. To help researchers to reach such optimal analytical conditions, α_h of representative rock-forming minerals and their wavelength dependence are presented in Table S6.

7.2. Correction methods of laser heating effects on Raman spectra

As the inclusion temperature during Raman spectroscopy increases concomitantly with increasing P_{ill}, the effect of laser heating on the Raman spectrum can be minimized by lowering P_{ill} to the greatest extent possible. However, the lowest P_{ill} does not mean that the laser heating effect on the Raman spectrum is completely absent. Therefore, depending on the situation, it is necessary to make some corrections to the measured data. In the following, we discuss how corrections should be made to the Raman spectral features when inclusions are suspected to be heated by a laser.

To illustrate the correction procedure, as an example, we measured Raman spectra of CO_2-rich fluid inclusions at various P_{ill}. The density of the fluid inclusions (ρ) was estimated from their peak positions. To ascertain the density of CO_2-rich fluid inclusion, several groups have improved Raman CO_2 densimeters and have demonstrated the density dependence of distance of Fermi diad splits ($\Delta = \nu^{+}_{F.\,D.} - \nu^{-}_{F.\,D.}$) (Fig. S1) (Rosso and Bodnar, 1995; Yamamoto et al., 2002; Kawakami et al., 2003; Yamamoto and Kagi, 2006; Song et al., 2009; Fall et al., 2011; Wang et al., 2011; Lamadrid et al., 2017; Yuan et al., 2017; Wang et al., 2019; Hagiwara et al., 2020; Le et al., 2020; Sublett et al., 2020). Therefore, ρ can be found from the measured Δ. However, because the relation between Δ and ρ depends on temperature, if the inclusions are heated to a considerable degree by the laser, then the obtained Δ must be corrected to ascertain a more reliable density specifically (e.g., Wang et al., 2019).

To derive a correction method, the relation between P_{ill} and Δ was investigated using the fluid inclusion in quartz (quartz01 fi56) and that in olivine (En2A oli02 fi13). The analysis was conducted using a grating

of 1800 grooves/mm; in all other respects, the analytical procedures are the same as those described in section 5.2. Analyses were conducted along both P_{ill} increasing (circle symbol) and decreasing (triangle symbol) cycles with four P_{ill} of 4.2, 7.7, 10.9, and 14.3 mW (Fig. 10). The measured Δ (Δ^{raw}) are first calibrated using measured and known distances between the Ne lines according to the explanation presented by Lamadrid et al. (2017) ($\Delta^{Ne\ calib}$ in Table 5). Subsequently, discrepancies in the calibration curves between laboratories were corrected by adding the correction term δ_Δ to $\Delta^{Ne\ calib}$. Finally, corrected Δ are defined as $\Delta^{Ne\ \&\ Qtz\ calib} = \Delta^{Ne\ calib} + \delta_\Delta$. δ_Δ was calculated using Eq. 10 of Hagiwara et al. (2020), Eq. 8 of Sublett et al. (2020), and the 8 $\Delta^{Ne\ calib}$ obtained from fluid inclusions in quartz. Detailed calculation processes of δ_Δ are shown in Table S7. The values of ρ_{Raman} calculated using substituting T_{sample} and $\Delta^{Ne\ \&\ Qtz\ calib}$ into Eq. 8 of Sublett et al. (2020) and P_{ill} at that time are presented in Table 5. The spectra were obtained five times at each P_{ill}. The mean values of $\Delta^{Ne\ \&\ Qtz\ calib}$ were presented in Fig. 10b. Their standard deviations (1σ) were shown as error bars.

The relations between P_{ill} and $\rho_{Th} - \rho_{Raman}$ are presented in Fig. 10a. The solid lines in Fig. 10a show a linear fit (York method) to eight data points. In the case of the inclusion in quartz, the slope was −0.00019 ± 0.00036 g/cm^3/mW, showing no significant positive or negative correlation with P_{ill}, at least in the studied P_{ill} range. As determined in this study, the *B* of fluid inclusion in quartz is about 0.01 °C/mW. Therefore, the expected laser-induced temperature rise is at most 0.2 °C. The Δ drop caused by laser heating is only 0.0006 cm^{-1}, which is well below the measurement precision of Δ. If no correlation exists between P_{ill} and the spectral features, then no correction is needed because the laser heating effect is negligible, at least within the studied P_{ill} range.

To ascertain whether spectral features of inclusions in a given mineral are unaffected by P_{ill}, it is desirable to select the inclusions that are most likely to be heated by the laser from all the inclusions to be analyzed. In other words, the fluid inclusions in the host mineral having the thickest and smallest diameter are optimal for evaluation. Some minerals have α_h varying with composition. The measurement of inclusions in such minerals must consider *B* differing in different compositional zones even in a single grain. Indeed, infrared studies of inclusions have revealed that even synthetic fluid inclusions in a single mineral grain, which are expected to have similar fluid composition and density, show different phase-transition temperatures depending on the compositions of the surrounding host phase (Casanova et al., 2018). Therefore, it is important to repeat this work (i.e., obtain the spectra of each inclusion while varying P_{ill}), even in a single crystal, if the host phase has significant compositional variation.

In the case of inclusion in olivine, the relation between $\rho_{Th} - \rho_{Raman}$ and P_{ill} shows a significant positive correlation; the slope was 0.0012 ± 0.0006 g/cm^3/mW (Fig. 10a). Earlier reports have described that even for fluids with constant density, ρ_{Raman} is underestimated as the temperature increases (Wang et al., 2011; Yuan et al., 2017; Wang et al., 2019; Sublett et al., 2020), which is consistent with our experimentally obtained results (Fig. 10a). Therefore, to obtain a more accurate ρ_{Raman}, the data must be measured using lower P_{ill} or corrected to account for the laser heating effect.

If the target spectral properties (here Δ) and temperature are almost linearly correlated at constant ρ, then the intercept of the linear fit between Δ and P_{ill} can be regarded as Δ at 0 mW. To verify the linearity of the relation between Δ and temperature at constant ρ, we calculated the relation between them at ρ = 0.698 g/cm^3 using Eq. 8 of Sublett et al. (2020). For the calculation, we assumed *B* = 1.1 °C/mW so that the obtained slope of the line in the calculations corresponds with that obtained from measured relation between Δ and P_{ill}. As a result, although their equation is not a linear function, it shows an almost linear relation at least within *P*–*T* of our interest (black line in Fig. 10a). Therefore, the intercept at the linear fit of the measured Δ (Δ = 104.283 ± 0.016 cm^{-1}) is regarded as being the true value corrected for the laser heating effect

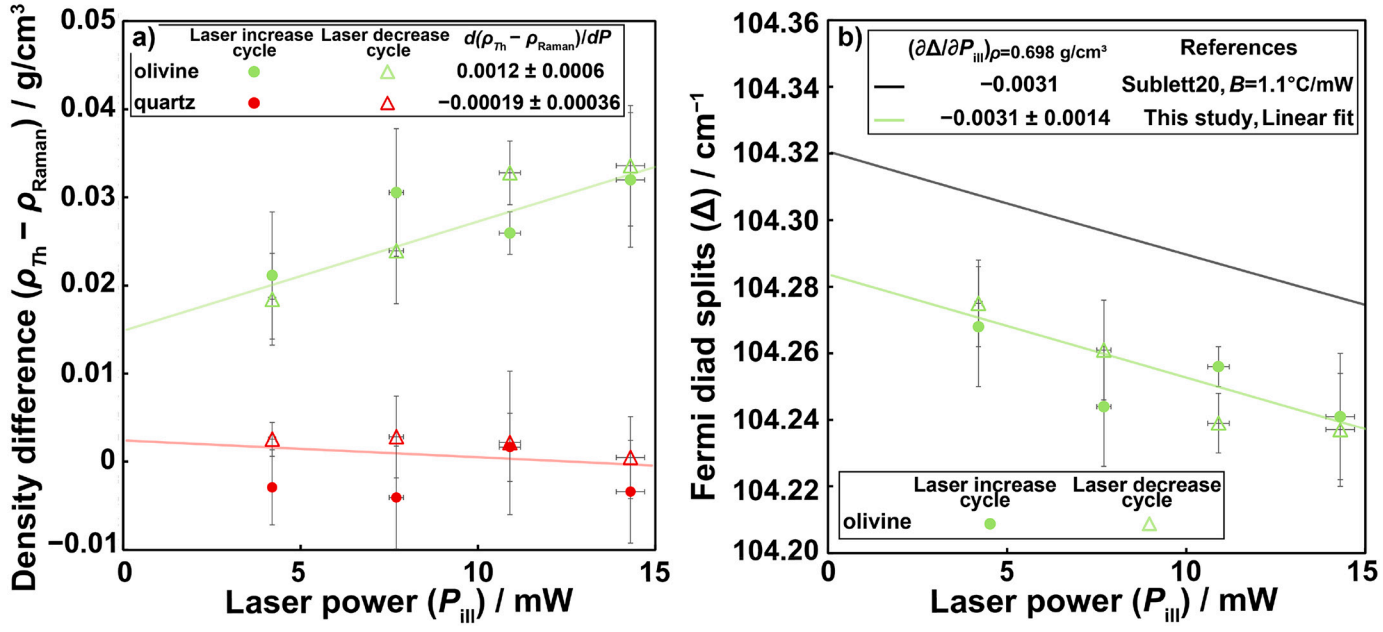

Fig. 10. a) Laser power dependence of the difference between the density of CO_2 calculated from the homogenization temperature (ρ_{Th}) and the density calculated from the Fermi diad splits (ρ_{Raman}). ρ_{Raman} was calculated by substituting $\Delta^{Ne\ \&\ Qtz\ calib}$ and the temperature monitored in Linkam stage into Eq. 8 of Sublett et al. (2020). The stage temperature and ρ_{Raman} are presented in Table 5. We measured fluid inclusions in olivine (olivine02 fi13) and quartz (quartz01 fi56), with data plotted respectively as green and red symbols. The measurements were made with the laser power increasing cycle (circle) and decreasing cycle (triangle). In the case of inclusions in olivine, ρ_{Raman} is underestimated with increasing laser power. However, in the case of inclusions in quartz, ρ_{Raman} was kept constant with increasing laser power. b) Relation between Δ of fluid inclusions in olivine (olivine02 fi13) and laser power. The green solid line shows the linear fit (York method) to eight data points. The line slope is −0.0031 ± 0.0014 cm^{-1}/mW. The black line represents calculated relations between laser power and Fermi diad split using Eq. 8 of Sublett et al. (2020). The sample temperature was assumed to be 27.2 °C with laser power of 0 mW. The calculated slopes of the relations between Δ and laser power at laser heating coefficients of 1.1 °C/mW were − 0.0031 cm^{-1}/mW. (For interpretation of the references to colour in this figure legend, the reader is referred to the web version of this article.)

Table 5
Measured fluid density, distance of Fermi diad splits, sample temperature, and laser power.

Sample	ρ_{Th}	P_{ill}	σ_{Pill}	T_{sample}	Δ^{raw}	$\Delta^{Ne\ calib}$	$\Delta^{Ne\ \&\ Qtz\ calib}$[a]	σ_{Δ}	ρ_{Raman}[b]	$\sigma_{\rho Raman}$[c]	$\rho_{Th} - \rho_{Raman}$
	g/cm^3	mW	mW	°C	cm^{-1}	cm^{-1}	cm^{-1}	cm^{-1}	g/cm^3	g/cm^3	g/cm^3
En2A oli02 fi13	0.698	4.2	0.1	27.2	104.168	104.181	104.268	0.018	0.6767	0.0072	0.0211
	0.698	7.7	0.2	27.4	104.144	104.157	104.244	0.018	0.6672	0.0072	0.0306
	0.698	10.9	0.3	27.2	104.157	104.169	104.256	0.006	0.6718	0.0024	0.0260
	0.698	14.3	0.4	27.2	104.144	104.154	104.241	0.019	0.6658	0.0076	0.0320
	0.698	14.3	0.4	27.2	104.137	104.150	104.237	0.017	0.6642	0.0068	0.0336
	0.698	10.9	0.3	27.2	104.139	104.152	104.239	0.009	0.6650	0.0036	0.0328
	0.698	7.7	0.2	27.2	104.162	104.174	104.261	0.015	0.6739	0.0060	0.0239
	0.698	4.2	0.1	27.1	104.174	104.188	104.275	0.013	0.6794	0.0052	0.0184
Quartz01 fi56	0.786	4.2	0.1	26.6	104.447	104.467	104.554	0.011	0.7887	0.0043	−0.0029
	0.786	7.7	0.2	26.9	104.454	104.469	104.556	0.015	0.7899	0.0058	−0.0041
	0.786	10.9	0.3	27.3	104.436	104.453	104.540	0.010	0.7842	0.0039	0.0016
	0.786	14.3	0.4	27.3	104.451	104.466	104.553	0.015	0.7892	0.0058	−0.0034
	0.786	14.3	0.4	27.3	104.442	104.456	104.543	0.012	0.7853	0.0047	0.0005
	0.786	10.9	0.3	27.2	104.439	104.452	104.539	0.021	0.7837	0.0082	0.0021
	0.786	7.7	0.2	27.3	104.438	104.450	104.537	0.012	0.7830	0.0047	0.0028
	0.786	4.2	0.1	27.2	104.437	104.451	104.538	0.005	0.7833	0.0019	0.0025

[a] $\Delta^{Ne\ \&\ Qtz\ calib}$ is defined as "$\Delta^{Ne\ calib} + \delta_{\Delta}$" cm^{-1}. δ_{Δ} can be found by optimizing Eq. 10 of Hagiwara et al. (2020) to the minimum and is determined as 0.087 cm^{-1}.
[b] ρ_{Raman} is density calculated by substituting T_{sample} and $\Delta^{Ne\ \&\ Qtz\ calib}$ into Eq. 8 of Sublett et al. (2020).
[c] $\sigma\rho_{Raman}$ is density error calculated by substituting T_{sample} and $\Delta^{Ne\ \&\ Qtz\ calib} + \sigma_{\Delta}$ into Eq. 8 of Sublett et al. (2020).

because Δ and P_{ill} is linearly correlated (Fig. 10a). Assuming that the error of the correction term δ_{Δ} determined in Table S7 is also 0.016 cm^{-1}, the final error of the obtained intercept is $\sqrt{0.016^2 + 0.016^2} = 0.023$ cm^{-1}. In addition, because the standard error of Eq. 8 of Sublett et al. (2020) is reported as ±0.006 g/cm^3, the error of Δ at 0.698 g/cm^3 is expected to be ±0.015 cm^{-1}, which is the difference of Δ obtained by Eq. 8 of Sublett et al. (2020) applied for the conditions of $\rho = 0.698$ g/cm^3 and $\rho = 0.704$ (or 0.692) g/cm^3 at the temperature of 27.2 °C. Therefore, deviation of measured intercept (Δ = 104.283 cm^{-1}) from calculated one (Δ = 104.321 cm^{-1}) is almost equal to the sum of the errors of the measured and calculated Δ. By this series of analyses, the laser heating effect on Δ of a single fluid inclusion can be corrected. However, if the relation between the Raman spectral properties and temperature is not linear in the *P–V–T–X* range of interest, then the intercept should be obtained by fitting with a function that best describes the relation.

However, it is very time-consuming to perform a series of operations (i.e., to obtain the spectra of each inclusion while varying P_{ill}) to estimate the intercept values for dozens of inclusions. Fortunately, however, if the temperature dependence of the calibration curve is known, then there is no need to repeat this series of operations if only *B* can be determined. This is true because, once *B* is known, the temperature of the inclusions in the analysis is calculable. We can correct the laser heating effect using a calibration curve with known temperature dependence. In the following, we explain how to estimate *B* from the relation between the Raman spectral features and P_{ill} of an inclusion when the temperature dependence of the calibration curve is known.

For a Raman CO_2 densimeter, the slope of the relation between Δ and P_{ill} ($\partial\Delta/\partial P_{ill}$) depends on ρ and *B*. Consequently, from the relation between Δ, ρ, and *T* obtained in an earlier study, *B* satisfying the measured $(\partial\Delta/\partial P_{ill})_{\rho}$ is obtainable. According to Eq. 8 of Sublett et al. (2020), *B* satisfying $(\partial\Delta/\partial P_{ill})_{\rho} = -0.0031 \pm 0.0014$ at $\rho = 0.698$ g/cm^3 is $B = 1.1 \pm 0.5$ °C/mW (Fig. 10a). This result is consistent with the actual *B* of oli02 fi13, $B_{Raman} = 0.6 \pm 0.3$ °C/mW (Table 4). Therefore, if the temperature dependence of the calibration curve is known, but *B* is unknown, then one can find *B* using the procedure described above. The precision of the measurement of *B* depends on the degree of temperature dependence of the calibration curve, but it is possible to determine *B* more accurately by performing the above series of analyses over a wider P_{ill} range. However, if the relation between temperature and target spectral feature at desired *P–V–T–X* conditions is unknown, then *B* cannot be estimated by the procedure described above. Therefore, under such conditions, the raw data should be corrected by estimating the value of the intercept from the relation between the Raman spectral features and P_{ill}.

To evaluate the effect of laser heating on the geological application of inclusion analysis, as an example, we consider an example of pressure estimation from a CO_2 fluid inclusion in a mantle xenolith. Oglialoro et al. (2017) showed the existence of a magma storage region located in the lower oceanic crust at a depth of 0.26–0.34 GPa beneath the El Hierro Volcano, Canary Islands, based on the density of CO_2-rich inclusions in mantle xenoliths. For example, when measuring Δ of a CO_2 fluid inclusion of 0.7 g/cm^3 in spinel assuming $P_{ill} = 10$ mW and $B = 6.0$ °C/mW, the inclusion temperature during the analysis reaches 85 °C; the Δ would drop by 0.16 cm^{-1} lower than the true value according to Eq. 8 of Sublett et al. (2020). Results show that the density obtained from the measured Δ is 0.636 g/cm^3, which is 9% lower than the true value. If we calculate the CO_2 trapping depth based on this density and assuming 1000 °C, then the result would be 0.28 GPa, which is 0.06 GPa lower than the true depth (0.34 GPa). Pressures are calculated following the method described by Pitzer and Sterner (1994). Because this deviation is much larger than the uncertainty of depth derived from the error in the temperature estimation (±30 °C corresponding to ±0.01 GPa), laser heating can be a major source of error. However, for inclusions with $B = 1.0$ °C/mW, such as those hosted in olivine and pyroxene, the underestimate of depth provenance is only 0.01 GPa, which is in similar range to the error derived from the temperature estimation. Therefore, the effect of laser heating is not so great. Therefore, although correcting the effects that laser heating will give data closer to the true values, such corrections are not necessarily required for the geological application when inclusions have small *B*.

Results of this study show that the use of the lowest P_{ill} can reduce the deviation of the measured Raman spectral feature from the true value. Therefore, the Raman data obtained under such conditions will be approximately equal to the true value. Corrections for the effects of laser heating are not always necessary because those effects depend on the quality of the data which the researcher desires. However, at least when comparing data obtained from different mineral species, the presence or absence of laser heating effect should be described. In addition, if the laser heating effect on the measured values is not negligible, we recommend reporting of how the ideal measurement conditions were reached and what corrections were made to the raw data to interpret them.

8. Conclusions

Experiments and heat transport simulations were combined to determine the laser heating coefficient (°C/mW) of the inclusions hosted in olivine, orthopyroxene, clinopyroxene, spinel, and quartz. We identify the influential parameters on the laser heating of the inclusions during Raman spectroscopic analysis. The experimental methods estimates B from the slope of the linear fitting of the inclusion temperature and P_{ill} obtained with a hot band thermometer.

The average B of inclusions in each host mineral was in the order of quartz << olivine < opx ≈ cpx < < spinel. Because this order is equal to the order of α_h, except that clinopyroxene and orthopyroxene are in reverse order, the most influential experimental parameter on B would be α_h, as suggested by earlier studies and our simulations. Aside from the α_h, the host mineral thickness and size and the heat transport at the boundaries can be the main factors that control B. Therefore, it is possible to reduce B to some extent by adjusting the shape of the host mineral during the sample preparation process. However, the radius and depth of inclusions have little effect on B if $\alpha_h > \alpha_{inc}$. Therefore, if researchers find that the physicochemical properties of inclusions measured by Raman spectroscopic analysis depend on the inclusion size or the distance from the sample surface, then laser heating can be excluded from the cause of that dependence.

For small host minerals and translucent minerals such as Cr-spinel, the temperature of the inclusions can rise tens or hundreds of degrees, even with the laser power typically used for inclusion analysis. For such situations in which the effects of laser heating are unavoidable, we propose some recommendations for the correction of laser heating effects on measured Raman spectra features. With such treatment, even if the Raman spectral features are altered by laser heating, results obtained from Raman spectroscopy become accurate.

Declaration of Competing Interest

The authors declare that they have no known competing financial interests or personal relationships that could have appeared to influence the work reported in this paper.

Acknowledgements

We thank Takashi Yoshino for him help in using joint-use facilities of the Institute for Planetary Materials, Okayama University. We thank Balz Kamber for editorial handling, and R. J. Bakker and an anonymous reviewer for constructive reviews that greatly improved this manuscript. This study was supported by Grants-in-Aid for Scientific Research (Nos. JP17K18794, JP17H02994, and JP16H04079 for JY, and JP19J21537 for YH) from the Japan Society for the Promotion of Science. The financial support was also provided by the Joint Usage/Research Program of ERI, the University of Tokyo (No. JURP2018-B-01).

Appendix A. Supplementary data

Supplementary data to this article can be found online at https://doi.org/10.1016/j.chemgeo.2020.119928.

References

Angel, R.J., Murri, M., Mihailova, B., Alvaro, M., 2019. Stress, strain and Raman shifts. Zeitschrift fur Krist.-Cryst. Mater. 234, 129–140.
Arakawa, M., Yamamoto, J., Kagi, H., 2008. Micro-Raman thermometer for CO_2 fluids: temperature and density dependence on Raman Spectra of CO_2 fluids. Chem. Lett. 37, 280–281.
Bakker, R.J., 2004. Raman spectra of fluid and crystal mixtures in the systems H_2O, H_2O–NaCl and H_2O–$MgCl_2$ at low temperatures: applications to fluid-inclusion research. Can. Mineral. 42, 1283–1314.
Beyssac, O., Goffé, B., Chopin, C., Rouzaud, J.N., 2002. Raman spectra of carbonaceous material in metasediments: a new geothermometer. J. Metamorph. Geol. 20, 859–871.
Branlund, J.M., Hofmeister, A.M., 2007. Thermal diffusivity of quartz to 1,000 °C: Effects of impurities and the α-β phase transition. Phys. Chem. Miner. 34, 581–595.
Casanova, V., Kouzmanov, K., Audétat, A., Wälle, M., Ubrig, N., Ortelli, M., Fontboté, L., 2018. Fluid inclusion studies in opaque ore minerals: II. A comparative study of syngenetic synthetic fluid inclusions hosted in quartz and opaque minerals. Econ. Geol. 113, 1861–1883.
Català, F., Marsà, F., Montes-Usategui, M., Farré, A., Martín-Badosa, E., 2017. Influence of experimental parameters on the laser heating of an optical trap. Sci. Rep. 7, 1–9.
Celliers, P.M., Conia, J., 2000. Measurement of localized heating in the focus of an optical trap. Appl. Opt. 39, 3396.
Chio, C.H., Sharma, S.K., Lucey, P.G., Muenow, D.W., 2003. Effects of particle size and laser-induced heating on the Raman spectra of alpha quartz grains. Appl. Spectrosc. 57, 774–783.
Everall, N.J., 2010. Confocal Raman microscopy: Common errors and artefacts. Analyst 135, 2512–2522.
Fall, A., Tattitch, B., Bodnar, R.J., 2011. Combined microthermometric and Raman spectroscopic technique to determine the salinity of H_2O–CO_2–NaCl fluid inclusions based on clathrate melting. Geochim. Cosmochim. Acta 75, 951–964.
Frezzotti, M.L., Tecce, F., Casagli, A., 2012. Raman spectroscopy for fluid inclusion analysis. J. Geochem. Explor. 112, 1–20.
Ghosh, G., 1999. Dispersion-equation coefficients for the refractive index and birefringence of calcite and quartz crystals. Opt. Commun. 163, 95–102.
Hagiwara, Y., Takahata, K., Torimoto, J., Yamamoto, J., 2018. CO_2 Raman thermometer improvement: comparing hot band and Stokes and anti-Stokes Raman scattering thermometers. J. Raman Spectrosc. 49, 1776–1781.
Hagiwara, Y., Torimoto, J., Yamamoto, J., 2020. Pressure measurement and detection of small H_2O amounts in high-pressure H_2O–CO_2 fluid up to 141 MPa using Fermi diad splits and bandwidths of CO_2. J. Raman Spectrosc. 51, 1003–1019.
Hansen, G.B., 1997. Spectral absorption of solid CO_2 from the ultraviolet to the far-infrared. Adv. Sp. Res. 20, 1613–1616.
Haro-González, P., Ramsay, W.T., Maestro, L.M., Del Rosal, B., Santacruz-Gomez, K., Iglesias-De La Cruz, M.D.C., Sanz-Rodríguez, F., Chooi, J.Y., Sevilla, P.R., Bettinelli, M., Choudhury, D., Kar, A.K., Solé, J.G., Jaque, D., Paterson, L., 2013. Quantum dot-based thermal spectroscopy and imaging of optically trapped microspheres and single cells. Small 9, 2162–2170.
Henry, D.G., Jarvis, I., Gillmore, G., Stephenson, M., 2019. Raman spectroscopy as a tool to determine the thermal maturity of organic matter: Application to sedimentary, metamorphic and structural geology. Earth Sci. Rev. 198, 102936.
Hofmeister, A.M., 2001. Thermal conductivity of spinels and olivines from vibrational spectroscopy: Ambient conditions. Am. Mineral. 86, 1188–1208.
Hofmeister, A.M., 2012. Thermal diffusivity of orthopyroxenes and protoenstatite as a function of temperature and chemical composition. Eur. J. Mineral. 24, 669–681.
Kagi, H., Tsuchida, I., Wakatsuki, M., Takahashi, K., Kamimura, N., Iuchi, K., Wada, H., 1994. Proper understanding of down-shifted Raman spectra of natural graphite: Direct estimation of laser-induced rise in sample temperature. Geochim. Cosmochim. Acta 58, 3527–3530.
Kawakami, Y., Yamamoto, J., Kagi, H., 2003. Micro-Raman densimeter for CO_2 inclusions in mantle- derived minerals. Appl. Spectrosc. 57, 1333–1339.
Khashan, M.A., Nassif, A.Y., 2001. Dispersion of the optical constants of quartz and polymethyl methacrylate glasses in a wide spectral range: 0.2–3 μm. Opt. Commun. 188, 129–139.
Kohn, M.J., 2014. "Thermoba-Raman-try": Calibration of spectroscopic barometers and thermometers for mineral inclusions. Earth Planet. Sci. Lett. 388, 187–196.
Lamadrid, H.M., Moore, L.R., Moncada, D., Rimstidt, J.D., Burruss, R.C., Bodnar, R.J., 2017. Reassessment of the Raman CO_2 densimeter. Chem. Geol. 450, 210–222.
Le, V.-H., Caumon, M.-C., Tarantola, A., Randi, A., Robert, P., Mullis, J., 2020. Calibration data for simultaneous determination of P–V–X properties of binary and ternary CO_2–CH_4–N_2 gas mixtures by Raman spectroscopy over 5–600 bar: Application to natural fluid inclusions. Chem. Geol. 552, 119783.
Linstrom, P.J., Mallard, W.G. (Eds.), 2020. NIST Chemistry WebBook, NIST Standard Reference Database Number 69. National Institute of Standards and Technology, Gaithersburg MD, p. 20899 (retrieved May 9, 2020).
Liu, Y., Cheng, D.K., Sonek, G.J., Berns, M.W., Chapman, C.F., Tromberg, B.J., 1995. Evidence for localized cell heating induced by infrared optical tweezers. Biophys. J. 68, 2137–2144.
Lucey, P.G., 1998. Model near-infrared optical constants of olivine and pyroxene of iron content. J. Geophys. Res. 103, 1703–1713.
Mao, H., Arias-Gonzalez, J.R., Smith Jr., S.B.I., Bustamante, C., 2005. Temperature Control Methods in a Laser Tweezers System. Biophys. J. 89, 1308–1316.
Maruyama, Y., Kanematsu, W., 2011. Confocal volume in laser Raman microscopy depth profiling. J. Appl. Phys. 110, 1–9.
Mazzucchelli, M.L., Burnley, P., Angel, R.J., Morganti, S., Domeneghetti, M.C., Alvaro, M., 2018. Elastic geothermobarometry: Corrections for the geometry of the host-inclusion system. Geology 46, 231–234.
Moore, L.R., Gazel, E., Tuohy, R., Lloyd, A.S., Esposito, R., Steele-MacInnis, M., Hauri, E. H., Wallace, P.J., Plank, T., Bodnar, R.J., 2015. Bubbles matter: an assessment of the contribution of vapor bubbles to melt inclusion volatile budgets. Am. Mineral. 100, 806–823.
Oglialoro, E., Frezzotti, M.L., Ferrando, S., Tiraboschi, C., Principe, C., Groppelli, G., Villa, I.M., 2017. Lithospheric magma dynamics beneath the El Hierro Volcano, Canary Islands: insights from fluid inclusions. Bull. Volcanol. 79.
Osako, M., Ito, E., Yoneda, A., 2004. Simultaneous measurements of thermal conductivity and thermal diffusivity for garnet and olivine under high pressure. Phys. Earth Planet. Inter. 143, 311–320.
Palik, E.D., 1998. Handbook of Optical Constants of Solids. Elsevier Science, USA.

Pegau, W.S., Gray, D., Zaneveld, J.R.V., 1997. Absorption and attenuation of visible and near-infrared light in water: dependence on temperature and salinity. Appl. Opt. 36, 6035.
Peterman, E.J.G., Gittes, F., Schmidt, C.F., 2003. Laser-induced heating in optical traps. Biophys. J. 84, 1308–1316.
Pitzer, K.S., Sterner, S.M., 1994. Equations of state valid continuously from zero to extreme pressures for H_2O and CO_2. J. Chem. Phys. 101, 3111–3116.
Rosso, K.M., Bodnar, R.J., 1995. Microthermometric and Raman spectroscopic detection limits of CO_2 in fluid inclusions and the Raman spectroscopic characterization of CO_2. Geochim. Cosmochim. Acta 59, 3961–3975.
Röttgers, R., McKee, D., Utschig, C., 2014. Temperature and salinity correction coefficients for light absorption by water in the visible to infrared spectral region. Opt. Express 22, 25093.
Song, Y., Chou, I., Hu, W., Burruss, R., Lu, W., 2009. CO_2 density-Raman shift relation derived from synthetic inclusions in fused silica capillaries and its application. Acta Geol. Sin. 83, 932–938.
Span, R., Wagner, W., 1996. A new EOS for CO_2 covering the fluid region from the triple point temperature to 1100 K at pressures up to 800 MPa. J. Phys. Chem. Ref. Data 25, 1509–1596.
Sublett, D.M., Sendula, E., Lamadrid, H., Steele-MacInnis, M., Spiekermann, G., Burruss, R.C., Bodnar, R.J., 2020. Shift in the Raman symmetric stretching band Shift in the Raman symmetric stretching band of N_2, CO_2, and CH_4 as a function of temperature, pressure, and density. J. Raman Spectrosc. 51, 555–568.
Taran, M.N., Langer, K., 2001. Electronic absorption spectra of Fe^{2+} ions in oxygen-based rock-forming minerals at temperatures between 297 and 600 K. Phys. Chem. Miner. 28, 199–210.
Taran, M.N., Matsyuk, S.S., 2013. Fe^{2+}, Mg-distribution among non-equivalent structural sites M1 and M2 in natural olivines: an optical spectroscopy study. Phys. Chem. Miner. 40, 309–318.
Taran, M.N., Ohashi, H., Langer, K., Vishnevskyy, A.A., 2011. High-pressure electronic absorption spectroscopy of natural and synthetic Cr^{3+}-bearing clinopyroxenes. Phys. Chem. Miner. 38, 345–356.
Taran, M.N., Parisi, F., Lenaz, D., Vishnevskyy, A.A., 2014. Synthetic and natural chromium-bearing spinels: an optical spectroscopy study. Phys. Chem. Miner. 41, 593–602.
Thompson, B.A., Harteck, P., Reeves, R.R., 1963. Ultraviolet absorption coefficients of CO_2, CO, O_2, H_2O, N_2O, NH_3, NO, SO_2, and CH_4 between 1850 and 4000 Å. J. Geophys. Res. 68, 6431–6436.
Umeda, H., Enami, M., 2014. Testing for robustness on estimation of graphitization degree by Raman spectroscopy. J. Mineral. Petrol. Sci. 109, 279–285.
Wang, C., Yoneda, A., Osako, M., Ito, E., Yoshino, T., Jin, Z., 2014. Measurement of thermal conductivity of omphacite, jadeite, and diopside up to 14 GPa and 1000 K: Implication for the role of eclogite in subduction slab. J. Geophys. Res. Solid Earth 6277–6287.
Wang, W., Caumon, M.-C., Tarantola, A., Pironon, J., Lu, W., Huang, Y., 2019. Raman spectroscopic densimeter for pure CO_2 and CO_2–H_2O–NaCl fluid systems over a wide P–T range up to 360 °C and 50 MPa. Chem. Geol. 528, 119281.
Wang, X., Chou, I.M., Hu, W., Burruss, R.C., Sun, Q., Song, Y., 2011. Raman spectroscopic measurements of CO_2 density: Experimental calibration with high-pressure optical cell (HPOC) and fused silica capillary capsule (FSCC) with application to fluid inclusion observations. Geochim. Cosmochim. Acta 75, 4080–4093.
Whitelaw, J., 1997. Convective Heat Transfer. Int. Encycl, Heat Mass Transf.
Yamamoto, J., Kagi, H., 2006. Extended Micro-Raman densimeter for CO_2 applicable to Mantle-originated fluid inclusions. Chem. Lett. 35, 610–611.
Yamamoto, J., Kagi, H., Kaneoka, I., Lai, Y., Prikhod'ko, V.S., Arai, S., 2002. Fossil pressures of fluid inclusions in mantle xenoliths exhibiting rheology of mantle minerals: Implications for the geobarometry of mantle minerals using micro-Raman spectroscopy. Earth Planet. Sci. Lett. 198, 511–519.
Yamamoto, J., Nishimura, K., Ishibashi, H., Kagi, H., Arai, S., Prikhod'ko, V.S., 2012. Thermal structure beneath Far Eastern Russia inferred from geothermobarometric analyses of mantle xenoliths: Direct evidence for high geothermal gradient in backarc lithosphere. Tectonophysics 554–557, 74–82.
Yuan, X., Mayanovic, R.A., Zheng, H., Sun, Q., 2017. Determination of pressure in aqueo-carbonic fluid inclusions at high temperatures from measured Raman frequency shifts of CO_2. Am. Mineral. 102, 404–411.
Zhong, X., Moulas, E., Tajčmanová, L., 2020. Post-entrapment modification of residual inclusion pressure and its implications for Raman elastic thermobarometry. Solid Earth 11, 223–240.